1 TITLE

2 Comparative proximity biotinylation produces an inventory of RAB18-interactions and

3 implicates RAB18 in cholesterol mobilization

4

5 RUNNING TITLE

6 GEF-dependent RAB18 interactions

7

8 AUTHORS

9 Robert S. Kiss*[1], Jarred Chicoine[1], Robert Sladek[1], He Chen[1], Alessandro Pisaturo[1],

10 Cyril Martin[1], Jessica D. Dale[2], Tegan A. Brudenell[2], Archith Kamath[3,4], Jimi C.

11 Wills[3], Alex von Kriegsheim[3], Tommy Nilsson[1], Eamonn Sheridan[2], Mark T.

12 Handley*[2]

13

14 AFFILIATIONS

15 [1]Research Institute of the McGill University Health Centre

16 1001 boul Decarie

17 Glen Site Block E

18 Montreal, QC

19 H4A 3J1

20 Canada

21

22 [2] Leeds Institute of Medical Research (LIMR)

23 St James's University Hospital

24 Leeds LS9 7TF

25   United Kingdom

26

27   [3]Cancer Research UK Edinburgh Centre

28   MRC Institute of Genetics & Molecular Medicine

29   The University of Edinburgh

30   Western General Hospital

31   Edinburgh EH4 2XR

32   United Kingdom

33

34   [4]Medical Sciences Division

35   University of Oxford

36   Oxford OX3 9DU

37   United Kingdom.

38

39   *authors contributed equally

40

41   CORRESPONDING AUTHORS

42   Robert S. Kiss: robert.kiss@mcgill.ca

43   Mark T. Handley: m.handley@leeds.ac.uk

44

45   KEYWORDS

46   RAB18, BioID, Cholesterol, SPG20, SEC22A, TMCO4

47

48   SUMMARY STATEMENT

49   We used proximity biotinylation together with guanine nucleotide exchange factor

50   (GEF)-null cell lines to discriminate functional RAB18-interactions. We anticipate that

51   this approach will be broadly applicable in small GTPase research.

52

53   ABSTRACT

54   Loss of functional RAB18 causes the autosomal recessive condition Warburg Micro

55   syndrome. To better understand this disease, we used proximity biotinylation in

56   HEK293 and HeLa cells to generate an inventory of potential RAB18 effectors. In

57   HeLa cells, we expressed BirA*-RAB18 in cells in which RAB18-guanine nucleotide

58   exchange factor (GEF) activity was disrupted with CRISPR. We found that most

59   RAB18-interactions are regulated independently by its different GEFs; the binary

60   RAB3GAP1-RAB3GAP2 complex and the TRAPPC9-containing TRAPPII complex.

61   RAB3GAP-dependent RAB18 interactions included a group of microtubule-

62   interacting/membrane shaping proteins, a group of proteins involved in membrane

63   tethering and docking, and a group of lipid-modifying/lipid transport proteins. We

64   demonstrate that GEF-dependent Rab-interactions are highly amenable to

65   interrogation by proximity biotinylation. Further, we provide confirmatory evidence for

66   several of the interactors (SPG20/SPART, SEC22A and TMCO4) as well as

67   functional evidence supporting a role for RAB18 in modulating the close apposition

68   of membranes and in cholesterol mobilization.

69

70   INTRODUCTION

71   Rab Proteins are a large subfamily of small GTPases with discrete roles in

72   coordinating membrane trafficking (Zhen and Stenmark, 2015). They associate with

73   cellular membranes as a result of their C-terminal prenylation and like other small

74   GTPases, adopt different conformations and enter into different protein-protein

75   interactions according to whether they are GDP-, or GTP-bound. For Rab proteins,

76   cycles of GTP binding and hydrolysis are accompanied by cycles of membrane

77   association and dissociation that serve to promote the targeting of particular Rab

78   protein isoforms to particular membrane compartments. Although they possess

79   some intrinsic GTP-hydrolysis activity, their *in vivo* nucleotide-bound state is tightly

80   governed in cells by two classes of regulatory proteins. Guanine-nucleotide

81   exchange factors (GEFs) catalyse the exchange of bound GDP for GTP while

82   GTPase-activating proteins (GAPs) promote the hydrolysis of bound GTP to GDP

83   (Lamber et al., 2019, Barr and Lambright, 2010). The dissociation of Rab proteins

84   from membranes is mediated by GDP-dissociation inhibitor (GDI) proteins. GDIs

85   sequester GDP-bound Rabs in the cytosol, and are also involved in their

86   reassociation with membranes (Zhen and Stenmark, 2015).

87   Rab proteins have a variety of roles in the regulation of processes required to confer

88   compositional identity to membranous organelles and to subdomains within them.

89   These include membrane remodelling and the establishment of membrane contact

90   sites (Bui et al., 2010, Raiborg et al., 2015, Rocha et al., 2009, Sobajima et al.,

91   2018). Where exchange between organelles is mediated by carrier vesicles, these

92   processes are important in vesicle budding and transport, tethering at the

93   appropriate target membrane, and fusion (Cai et al., 2007). Under other

94   circumstances, membrane contact sites may be established to mediate direct fusion

95   between organelles or to facilitate the transfer of lipids and ions (Wu et al., 2018,

96   Langemeyer et al., 2018, Wickner, 2010). Rab proteins fulfil their roles by way of

97   protein-protein interactions with interacting partners termed 'effectors'. These

98   comprise an array of phylogenetically unrelated protein classes and can serve a

99   range of molecular functions. As such, they are most usually identified biochemically.

100   Biochemical identification of Rab effectors is challenging; Rab-effector interactions

101   are usually GTP-dependent and are often highly transient. Immunoprecipitation,

102   affinity purification and yeast-2-hybrid approaches have each been used but may be

103   more or less effective depending on the Rab isoform studied (Christoforidis et al.,

104   1999, Fukuda et al., 2008). One newer approach that has yielded identification of a

105   number of novel interactions is 'BioID' proximity biotinylation utilizing Rab proteins

106   fused to mutant forms of the promiscuous biotin ligase BirA*; the Rab fusion protein

107   biotinylates proximal proteins which are then purified on streptavidin and identified

108   through mass spectrometry (Gillingham et al., 2019, Liu et al., 2018, Roux et al.,

109   2012). Biotin labelling occurs in a relatively physiological context, and prospective

110   effectors can be purified under high stringency conditions. However, a drawback of

111   the technique is that it does not discriminate between close associations resulting

112   from functional protein-protein interactions and those resulting from overlapping

113   localizations.

114   RAB18 is a ubiquitously expressed ancestral Rab protein that localizes to the *cis*-

115   Golgi, endoplasmic reticulum (ER) and lipid droplets (LDs)(Martin et al., 2005, Ozeki

116   et al., 2005, Gerondopoulos et al., 2014, Handley et al., 2015). Previous work has

117   suggested that it functions in the regulation of lipolysis, and lipogenesis (Martin et al.,

118   2005, Ozeki et al., 2005, Pulido et al., 2011), trafficking between the Golgi and

119   endoplasmic reticulum (ER) (Dejgaard et al., 2008, Handley et al., 2015), ER

120   structure (Gerondopoulos et al., 2014), exocytosis (Vazquez-Martinez et al., 2007)

121   and autophagy (Bekbulat et al., 2018, Feldmann et al., 2017). RAB18 deficiency or

122   its dysregulation cause the autosomal recessive condition Warburg Micro syndrome

123   (Aligianis et al., 2005, Bem et al., 2011, Borck et al., 2011, Handley and Sheridan,

124   2018, Liegel et al., 2013)(MIMs 600118, 614222, 614225, 615663, 212720).

125   In order to address how RAB18 coordinates and performs its roles, we used BioID to

126   generate an inventory of its potential effectors. To discriminate functional

127   interactions, we used complementary comparative analyses in HEK293 and HeLa

128   cells. Known RAB18 effectors were more strongly labelled by a fusion of BirA* and

129   wild-type RAB18 than by one incorporating an inactive form, RAB18(Ser22Asn),

130   which is deficient in nucleotide-binding. Similarly, BirA*-RAB18 labelled known

131   effectors more strongly in wild-type cells than in cells in which RAB18-GEF activity

132   was disrupted with CRISPR. Interestingly, disruption of different GEF complexes

133   largely affected different sets of RAB18 interactions.

134   A restricted set of interactions were dependent on the binary RAB18-GEF complex

135   made up of RAB3GAP1 and RAB3GAP2 (Gerondopoulos et al., 2014). These

136   included known and novel interactors in discrete functional groups. We present direct

137   validation for several examples including the microtubule-binding protein

138   SPG20/SPART, the SNARE protein homologue SEC22A and an orphan lipase

139   TMCO4. Our data strongly support a previous suggestion (Xu et al., 2018) that

140   RAB18 effectors act collectively in lipid mobilization. The combined data elaborate a

141   model for RAB18 function and provide groundwork for future investigations. In

142   particular, a putative role in cholesterol mobilization and biosynthesis is highlighted.

143

144   RESULTS

145

146   An inventory of nucleotide-binding-dependent RAB18-associated proteins in HEK293

147   cells

148   We first generated HEK293 cells stably expressing BirA*-tagged fusion proteins of

149   wild-type RAB18, nucleotide-binding deficient RAB18(Ser22Asn) or GTP-hydrolysis

150   deficient RAB18(Gln67Leu) using the Flp-In system. We then carried out proximity-

151   labelling, affinity purification and mass spectrometry of biotinylated proteins as

152   previously described (Roux et al., 2018, Roux et al., 2012). Following removal from

153   the dataset of previously identified non-specific binders from an in-house database, a

154   total of 98 proteins were identified as associating with RAB18 across all samples

155   (see Table S1).

156   The most comprehensive annotation of candidate RAB18 effectors thus far was

157   made in the 2014 paper by Gillingham et al., which utilized an affinity purification-

158   mass spectrometry (AP-MS) approach and the *Drosophila* RAB18 orthologue

159   (Gillingham et al., 2014). In that study, a total of 456 proteins were identified as

160   interacting with RAB18. However, only 14 of these were well represented in terms of

161   spectral counts, exhibited low non-specific binding to GST/Sepharose and showed

162   low binding to other Rab protein isoforms. We took these 14 proteins as the most

163   plausible physiological RAB18 interactors. Orthologues of 7 of these 14 proteins

164   were also represented in our BioID data. The number of spectral counts recorded for

165   these 7 proteins did not clearly distinguish them from the remainder of this BioID

166   dataset. We therefore proceeded by comparing their differential labelling by the

167   different RAB18 fusion proteins.

168   We began analyses by exploring the possibility that BirA*-RAB18(Gln67Leu) fusion

169   protein would produce enhanced biotinylation of RAB18-effectors (as compared to

170   BirA*-RAB18(WT)). We normalized total spectral counts between the BirA*-

171   RAB18(Gln67Leu) and BirA*-RAB18(WT) datasets and then calculated mutant:wild-

172   type ratios for each RAB18-associated protein (Table S1). Association ratios for

173   known RAB18-interactors ranged from 0.1-1.49 indicating that RAB18 associations

174   were altered by the Gln67Leu variant, but not predictably so.

175   We next compared the BirA*-RAB18(Ser22Asn) and BirA*-RAB18(WT) datasets

176   (Figure 1, Table S1). The RAB18-GEF subunits RAB3GAP1 and RAB3GAP2

177   showed association ratios >1 consistent with the high affinity of Rab-GEFs for

178   cognate Rabs in their nucleotide-free state. Since most effector-interactions are

179   GTP-dependent, we ranked other prospective RAB18-interactors according to those

180   that showed the lowest association ratios. Figure 1B shows the 28 of 98 proteins

181   with BirA*-RAB18:BirA*-RAB18(Ser22Asn) association ratios <0.5. These include

182   the remaining 5 common interactors from the Gillingham et al. study, several of

183   which have association ratios of zero, indicating that labelling by BirA*-

184   RAB18(Ser22Asn) was absent. These data suggest that comparison of labelling by

185   wild-type and nucleotide-binding-deficient BirA*-Rab fusion proteins can be an

186   effective means to distinguish putative effectors.

187

188   <u>An inventory of RAB18-GEF-dependent RAB18-associated proteins in HeLa cells</u>

189   We had previously used CRISPR to generate a panel of clonal, otherwise isogenic,

190   HeLa cell lines, null for RAB18 and a number of its regulators (see Figure S1).

191   Having shown that the BirA*-RAB18(WT):BirA*-RAB18(Ser22Asn) comparison in

192   HEK293 cells was informative, we carried out similar comparisons between BioID-

193   labelling in wild-type and RAB18-GEF deficient HeLa cells (Figure 2A). Since GEF

194   activity promotes Rab GTP binding, and this is usually necessary for effector

195   interactions, these interactions would be attenuated in GEF-null cells. RAB3GAP1

196   and RAB3GAP2 are each essential subunits of a binary RAB18-GEF complex

197   whereas TRAPPC9 is reported to be essential for the RAB18-GEF activity of a

198   different GEF, the multisubunit TRAPPII complex (Gerondopoulos et al., 2014, Li et

199   al., 2017). We therefore carried out proximity labelling using transient expression of

200   the same exogenous BirA*-RAB18 construct in wild-type cells and in RAB3GAP1-,

201   RAB3GAP2- and TRAPPC9-null cell lines.

202   Prior to mass-spec analysis, samples from each of the streptavidin pull-downs were

203   subjected to Western blotting to ensure comparable BirA*-RAB18 expression (Figure

204   S2A). Label-free quantitative proteomics analyses were used to calculate 'LFQ

205   intensities' (Cox et al., 2014) for each RAB18-associated protein, which were then

206   normalized in each experiment according to the quantity of RAB18 found in each

207 sample. Samples from three independent experiments were analysed, and pull-down

208 samples from untransfected biotin-treated cells were used as controls in each case.

209 After filtering the data to remove known mass-spec contaminants, and any protein

210 identified at a high level in control samples, a total of 584, 483 and 506 RAB18-

211 associated proteins were identified in each experiment. A total of 457 proteins were

212 present in two or more of the replicate experiments (see Table S2). Orthologues of

213 10 of the 14 putative RAB18-interacting proteins identified by Gillingham et al. were

214 identified in the HeLa cell BioID dataset including all 7 of those also identified in the

215 HEK293 cell dataset. However, as in that dataset, these were not distinguished by

216 their comparative abundance.

217 Different Rab-GEF complexes may operate in distinct subcellular localizations and

218 coordinate associations with different effectors (Carney et al., 2006). Therefore, we

219 assessed whether non-zero intensities for each RAB18-associated protein correlated

220 between samples (Figure 2B, Figure S2B). Very strong correlations between protein

221 intensities from RAB3GAP1- and RAB3GAP2-null cells indicated that loss of either

222 protein had a functionally equivalent effect (R^2=0.99, see Figure 2B). In contrast,

223 intensities from RAB3GAP1- and TRAPPC9-null cells were much more poorly

224 correlated (R^2=0.73, see Figure S2B). We therefore considered RAB3GAP- and

225 TRAPPC9-dependent RAB18-associations separately.

226 Of the 457 proteins identified in two or more independent experiments, only 25

227 showed an association ratio <0.5 in the absence of functional RAB3GAP (Figure 2C-

228 D). These included orthologues of 9 of the 10 proteins identified in the Gillingham et

229 al. study. Thus, our approach was extremely powerful in discriminating putative

230 effector proteins. 133 proteins showed an association ratio <0.5 in the absence of

231 functional TRAPPC9 including the remaining common RAB18-interactor from the

232 Gillingham et al. study (see Table S2). There was only limited overlap between

233 RAB3GAP- and TRAPPC9-dependent associations (Figure 2C). Indeed, among the

234 28 nucleotide-binding-dependent RAB18 associations identified in HEK293 cells, 6

235 were also RAB3GAP-dependent, and 7 were TRAPPC9-dependent in HeLa cells

236 respectively, but none were both (Figure 1B). Among the 25 RAB3GAP-dependent

237 associations in HeLa cells, only 5 were also TRAPPC9 dependent (Figure 2C, Table

238 S2).

239   One of the TRAPPC9-dependent RAB18 associations was that with TBC1D5, a Tre-
240   2/Bub/Cdc16 (TBC) domain-containing RAB-GAP with a well characterised role in
241   regulation of RAB7 (Jia et al., 2016, Jimenez-Orgaz et al., 2018, Seaman et al.,
242   2009). This was a strong candidate as a RAB18 regulator or effector since it had
243   also been identified in the HEK293 dataset as well as in several previous studies
244   (Gillingham et al., 2019, Gillingham et al., 2014). We generated TBC1D5-null HeLa
245   cells, and first tested whether RAB7 and RAB18 dynamics were altered in these cells
246   using fluorescence recovery after photobleaching (FRAP). RAB7 dynamics were
247   substantially different in the TBC1D5-null cells as compared to those in wild-type
248   cells, consistent with reduced RAB7 GTP-hydrolysis resulting in its reduced GDI-
249   mediated exchange between membrane and cytosolic compartments (Figure S3A).
250   In contrast, RAB18 dynamics were unchanged in TBC1D5-null cells compared to
251   controls (Figure S3B). Further, RAB7 dynamics were unchanged in RAB18-null cells
252   compared to controls, indicating that RAB18 is not required for TBC1D5 activity
253   (Figure S3A). These data do not exclude TBC1D5 as a potential RAB18 effector, but
254   argue against a role for RAB18 in RAB7-regulation under resting conditions.

255

256   <u>Validation screening of RAB3GAP-dependent RAB18 associations</u>

257   Our continued study focused on the 25 RAB3GAP-dependent RAB18 associations
258   identified in HeLa cells on the basis that these included the majority of known RAB18
259   effectors together with a number of promising candidate effectors not previously
260   identified. Encouragingly, many of them also appear to share interconnected
261   functions and fell into three main groups (Figure 2D). A group of proteins involved in
262   membrane shaping, cytoskeletal remodelling and in membrane-microtubule contacts
263   included SPG20, BICD2, REEP4, CAMSAP1 and FAM134B. Of these, SPG20 was
264   previously found to interact with RAB18 (Gillingham et al., 2014), BICD2 interacts
265   with RAB18 among a number of Rab isoforms (Gillingham et al., 2019, Gillingham et
266   al., 2014) and REEP4 was previously shown to interact with RAB3GAP (Tinti et al.,
267   2012). Although not previously linked to RAB18, CAMSAP1 and FAM134B were
268   each identified in both HEK293 and HeLa datasets. Next, a group of proteins
269   involved in establishing membrane contacts included components of the NRZ/Dsl1
270   membrane-tethering complex, ZW10, RINT1 and NBAS, the Sec1/Munc18 (SM)
271   protein SCFD2 and SNAP-REceptor (SNARE) proteins STX18 and BNIP1. These

272   proteins have been previously studied in the context of RAB18 (Gillingham et al.,

273   2019, Gillingham et al., 2014, Li et al., 2019, Xu et al., 2018, Zhao and Imperiale,

274   2017). Also in this group were the SNARE protein homologue SEC22A and the ER-

275   resident multispanning transmembrane protein WFS1, which regulates membrane

276   contacts between the ER and mitochondria (Angebault et al., 2018). These latter

277   proteins had not been linked to RAB18 previously. The third group of proteins

278   associated with RAB18 were a number of lipid transport, exchange and modifying

279   proteins, C2CD2L, C2CD2, ORP2/OSBPL2, INPP5B, EBP and TMCO4.

280   Interestingly, all but TMCO4 have related lipid species as their known substrates.

281   C2CD2 and C2CD2L are thought to mediate phosphatidylinositol (PI) transfer

282   between apposed membranes (Lees et al., 2017), ORP2 has recently been shown to

283   exchange $PI(4,5)P_2$ and cholesterol and INPP5B hydrolyses $PI(4,5)P_2$ to $PI(4)P$

284   (Wang et al., 2019). EBP is a D8-D7 Sterol Isomerase involved in cholesterol

285   biosynthesis (Silve et al., 1996). Various members of the OSBP family interact with

286   Rab proteins (Gillingham et al., 2019, Johansson et al., 2005), and a number of Rab

287   isoforms interact with INPP5B (Fukuda et al., 2008, Williams et al., 2007), though

288   associations with RAB18 have not been previously reported.

289   For initial validation of our HeLa dataset, we first carried out an additional

290   independent BioID experiment with wild-type and RAB3GAP1-null cells and

291   subjected the resulting samples to Western blotting for selected RAB18-associated

292   proteins (Figure 3A). As with the mass spectrometry, these proteins showed either

293   complete (RAB3GAP1, RAB3GAP2, ZW10) or partial (SPG20, STX18) dependence

294   on RAB3GAP for their RAB18 association.

295   Since RAB18 and its regulators are linked to Warburg Micro syndrome, we next

296   asked whether the putative RAB18 effectors were linked to any diseases with

297   overlapping clinical features (Figure 3B). Micro syndrome is a clinically distinctive

298   disorder characterised by intellectual disability (ID), postnatal microcephaly, brain

299   malformations, ascending spastic paraplegia, neuropathy, hypogonadism and eye

300   abnormalities that include congenital bilateral cataracts, microphthalmia,

301   microcornea and optic atrophy (Handley and Sheridan, 2018). Among the

302   RAB3GAP-dependent RAB18 associations identified in the BioID screen, we noted

303   that several are encoded by disease-associated genes or their homologues. In

304   common with Micro syndrome, diseases linked to *SPG20*, *BICD2*, and the *REEP4-*

305   homologues *REEP1* and *REEP2* are associated with ascending paraplegia

306   (hereditary spastic paraplegia/HSP). *FAM134B* is associated with sensory and

307   autonomic neuropathy, while the eye features of Micro syndrome overlap a different

308   set of genes. *EBP* is linked to microphthalmia, microcornea and cataracts as well as

309   to brain malformations like those in Micro syndrome. Both *WFS1* and *NBAS* have

310   been linked to conditions associated with optic atrophy, and both *WFS1* and the

311   INPP5B homologue OCRL1 are linked to conditions associated with congenital

312   cataracts.

313   Given the suggestive convergences in protein function and gene-disease-

314   associations, we proceeded to examine the subcellular localizations of 12 putative

315   effectors for which antibodies were available (Figure 3C-D). To determine whether

316   the localization of these proteins was altered in cells lacking RAB18, we analysed

317   wild type and RAB18-null lines in each case. In order to directly compare cells of

318   different genotypes under otherwise identical conditions, we labelled them with

319   CellTrace-Violet and CellTrace-Far Red reagents before seeding, immunostaining

320   and imaging them together. Since RAB18 can localize to LDs, we analysed both

321   untreated cells (Figure 3C) and cells loaded with oleic acid and labelled with

322   BODIPY-558/568-C12 (Figure 3D).

323   We observed a variety of staining patterns for the different putative effector proteins.

324   These ranged from staining that was enriched at the perinuclear region of cells, to

325   staining that appeared reticular, to staining that appeared more diffuse (Figure 3C).

326   Each staining pattern was compatible with the known localization of RAB18, which is

327   distributed between *cis*-Golgi, ER and cytosolic compartments (Handley et al., 2015).

328   Staining patterns for individual proteins were similar in the HeLa cells and also in

329   wild-type and RAB18-null RPE1 cells generated to provide biological replicates

330   (Figure S4). In lipid-loaded cells, we observed that the localizations of proteins with

331   reticular staining patterns overlapped with LDs, but they did not obviously shift to

332   adopt an LD localization. However, the two proteins that showed the most diffuse

333   staining patterns in untreated cells - ZW10 and SPG20 - appeared enriched in the

334   vicinity of LDs in lipid-loaded cells (Figure 3D).

335   We saw no evidence for dramatic changes in protein localizations in RAB18-null

336   cells as compared to their wild-type counterparts. Fluorescence intensities in RAB18-

337   null and wild-type cells were also generally similar, except in the case of staining for

338   SPG20, in which it appeared lower in RAB18-null HeLa cells than in wild-type cells

339   (Figure 3C).

340

341   <u>Levels of SPG20 are significantly reduced in RAB18-null and TBC1D20-null cells</u>

342   In a RAB18-null mouse model of Warburg Micro syndrome, peripheral nerves have a

343   disordered cytoskeleton, and there is a striking accumulation of microtubules at

344   motor nerve terminals (Carpanini et al., 2014). Therefore, interactions between

345   RAB18 and microtubule-binding proteins is of particular interest. To confirm the

346   reduction in levels of SPG20 we observed in RAB18-null HeLa cells, we used

347   quantitative fluorescence microscopy (Figure 4A-C). The SPG20 antibody used in

348   this study has previously been used for this purpose (Nicholson et al., 2015).

349   However, to confirm its specificity and also to determine the levels of non-specific

350   background produced in our experiments, we first analysed SPG20-null cells (Figure

351   4A-B). Measured fluorescence intensity of SPG20-null cells provided a baseline

352   level, above which fluorescence levels are proportional to levels of SPG20. In

353   RAB18-null cells, SPG20 fluorescence was reduced to 67.16±3.77% (s.e.m.,

354   p<0.001) of that in wild-type cells (Figure 4C).

355   To determine whether levels of SPG20 were altered by disrupted RAB18 regulation,

356   we next compared SPG20 fluorescence of wild type, RAB3GAP1-, RAB3GAP2- and

357   TBC1D20-null cells. Loss of the RAB18-GEF subunits RAB3GAP1 or RAB3GAP2

358   did not significantly affect levels of SPG20, whereas loss of the RAB18-GAP

359   TBC1D20 led to a reduction comparable to that in RAB18-null cells (57.48%±2.57

360   (s.e.m., p<0.00005). To rule-out the possibility that reduced SPG20 levels in RAB18-

361   and TBC1D20-null HeLa cells were the result of clonal variation, we analysed the

362   corresponding panel of RPE1 cell lines. However, because the RPE1 cells were less

363   amenable to comparative immunofluorescence experiments than HeLa cells, we

364   used LFQ analysis of whole cell lysates. As in the HeLa cells, levels of SPG20 were

365   significantly reduced in RAB18- and TBC1D20-null RPE1 cells compared to wild-

366   type controls (p<0.05 following FDR correction), but not in the other genotypes

367   tested (Figure 4D, Table S3).

368   RAB18, TBC1D20 and the RAB3GAP complex have all been linked to roles in

369   proteostasis and autophagy (Bekbulat et al., 2018, Feldmann et al., 2017, Sidjanin et

370   al., 2016, Spang et al., 2014). It was therefore possible that reduced SPG20 levels in

371   RAB18- and TBC1D20-null cells were the result of widespread dysregulation of

372   proteostasis. To assess this possibility, we compared LFQ data from wild-type and

373   TBC1D20-null RPE1 and HeLa cells (Tables S3 and S4). Following FDR correction,

374   only a small number of proteins showed significantly altered levels in each cell type

375   and there was limited overlap between cell types. This is in-line with a recent study

376   showing a compensatory mechanism maintains levels of basal autophagy when

377   RAB18 is absent or dysregulated (Bekbulat et al., 2018). Thus, dysregulation of

378   SPG20 levels most likely arises from a discrete mechanism.

379   Discrete changes in SPG20 levels in RAB18- and TBC1D20-null cells together with

380   the previous report of a RAB18-SPG20 interaction (Gillingham et al., 2014) provided

381   strong evidence for a functional relationship between these proteins. We therefore

382   carried out co-expression experiments to determine whether they colocalize in cells.

383   Coexpression of mCherry-RAB18 and mEmerald-SPG20 in HeLa cells showed that,

384   as previously reported, mCherry-RAB18 adopts a largely reticular localization

385   (Gerondopoulos et al., 2014) whereas mEmerald-SPG20 appears largely diffuse

386   (Eastman et al., 2009)(Figure 4E). We did not observe any clear colocalization

387   between the proteins or any relocalization of mEmerald-SPG20 in cells expressing

388   mCherry-RAB18. Since both RAB18 and SPG20 localize to LDs, we next explored

389   whether the localization of either protein to LDs was dependent on the other. In oleic

390   acid/BODIPY-558/568-C12-loaded HeLa cells, we found that mEmerald-SPG20

391   became concentrated around LDs, but that its localization was similar in both wild-

392   type and RAB18-null cells (Figure 4F, left panels). Similarly, EGFP-RAB18 was

393   enriched around LDs in both wild-type and SPG20-null cells (Figure 4F, right

394   panels).

395   Collectively, our findings suggest that RAB18 and SPG20 become localized to LDs

396   independently, and that any RAB18-SPG20 interaction is likely to be transient. The

397   reduced levels of SPG20 in RAB18- and TBC1D20-null cells seem likely to result

398   from its reduced stability, and it is intriguing that a transient interaction could

399   influence this. Nevertheless, this is consistent with the involvement of TBC1D20-

400   catalysed RAB18 GTP-hydrolysis and accompanying conformational change.

401

402 <u>SEC22A associates with RAB18 and its knockdown causes altered LD morphology</u>

403 The most studied group of RAB18 effector proteins to date are the tethering factors

404 ZW10, NBAS and RINT1, which together comprise the NRZ/Dsl1 complex

405 (Gillingham et al., 2014, Li et al., 2019, Xu et al., 2018, Zhao and Imperiale, 2017).

406 The NRZ complex regulates assembly of an ER SNARE complex containing STX18.

407 The canonical, fusogenic, form of this complex contains STX18, BNIP1, USE1 and

408 SEC22B (Spang, 2012, Tagaya et al., 2014). However, it has been proposed that

409 SEC22B is dispensable for the functions of RAB18, the NRZ complex, STX18,

410 BNIP1 and USE1 in regulating LDs (Xu et al., 2018). Rather than promoting

411 membrane fusion it is suggested that, in the absence of SEC22B, these proteins can

412 mediate the close apposition of membranes to facilitate lipid transfer.

413 In the HEK293 and HeLa BioID datasets, RAB18-associations with all three NRZ

414 components were nucleotide-binding-dependent and RAB3GAP-dependent

415 respectively (Figures 1B, 2D, Tables S1, S2). In the HeLa dataset, the ER SNARE

416 proteins STX18 and BNIP1 were also identified as associating with RAB18 in a

417 RAB3GAP-dependent manner (Figure 2D, Table S2). Interestingly, also among the

418 RAB3GAP-dependent RAB18 associations was SEC22A, a poorly studied

419 homologue of SEC22B.

420 SEC22A is one of two SEC22B homologues in humans, the other being SEC22C.

421 Like SEC22B, SEC22A and SEC22C possess N-terminal Longin domains and C-

422 terminal transmembrane (TM) domains. However, they lack the central coiled-coil

423 SNARE domain through which SEC22B mediates membrane fusion as part of the

424 STX18 complex. SEC22B localizes to the ER–Golgi intermediate compartment,

425 whereas different isoforms of SEC22C localize to the ER or *cis*-Golgi (Yamamoto et

426 al., 2017, Ge et al., 2013, Zhang et al., 1999). The localization of SEC22A had not

427 been addressed. In the absence of commercially available antibodies for SEC22A,

428 we examined its localization through expression of an mEmerald-SEC22A fusion

429 protein (Figure 5A). mEmerald-SEC22A produced a characteristic reticular staining

430 pattern and colocalized with an exogenous ER marker suggesting that SEC22A

431 localizes to the ER.

432 We next sought to compare the localization of SEC22A and RAB18 and to determine

433 whether they interact. However, coexpression of mEmerald-SEC22A and mCherry-

434   RAB18 appeared to disrupt normal ER morphology and to produce vesicular

435   structures and inclusions positive for both proteins (Figure S5). Although this was not

436   inconsistent with a protein-protein interaction, it precluded the use of coexpressed

437   exogenous proteins to test such an interaction. We therefore used a BirA*-SEC22A

438   fusion protein to verify the RAB18-SEC22A association, to identify other SEC22A-

439   associations, and to determine whether these associations were influenced by the

440   absence of RAB18 or its regulators. To minimize potential toxicity while increasing

441   biotin-ligase activity, we used BioID2 (Kim et al., 2016) with a p.Gly40Ser active site

442   modification (Branon et al., 2018) and reduced biotin incubation time to 6 hours. LFQ

443   analysis following streptavidin pull-down and mass spectrometry indicated that

444   BioID2(Gly40S)-SEC22A was present at much lower levels than the BirA*-RAB18 in

445   the prior experiments (3.79±0.96%). However, after adjusting for non-specific binding

446   and normalizing the data according to the quantity of BioID2(Gly40S)-SEC22A in

447   each sample, the construct appeared to label RAB18 in a RAB3GAP-dependent

448   manner (Figure 5B). RAB3GAP1 and RAB3GAP2, as well as the putative RAB18-

449   associated proteins REEP4 and BICD2, were among 55 SEC22A-associated

450   proteins present in samples from wild-type cells in >2 replicate experiments and

451   represented by >3 spectral counts (Table S5). Furthermore, also among these

452   proteins, a subset of 9 SEC22A-associations were attenuated (association ratios

453   <0.5) in samples from both RAB18-null and RAB3GAP-null cells. Broadly, these data

454   were consistent with a functional SEC22A-RAB18 interaction.

455   Given the involvement of RAB18, the NRZ complex, and a STX18 complex lacking

456   SEC22B in the regulation of LDs, we asked whether SEC22A might also be involved.

457   Multiple studies have shown that LD morphology is altered in lipid-loaded cells in

458   which RAB18 expression - or that of its regulators - is disrupted or silenced, with

459   fewer and/or larger LDs are observed in these cells compared to controls (Bekbulat

460   et al., 2018, Carpanini et al., 2014, Gerondopoulos et al., 2014, Li et al., 2017, Liegel

461   et al., 2013, Xu et al., 2018). Similar observations have been made in ZW10-, NBAS-

462   , STX18-, BNIP1- and USE1-null cells, whereas LD size distribution is unaltered

463   when SEC22B expression is silenced (Xu et al., 2018). We examined the effects of

464   silencing ZW10, NBAS and SEC22A in oleic acid-loaded induced human hepatocyte

465   (IHH) cells (Figure 5C). ZW10 and NBAS silencing provided positive controls. ZW10

466   silencing led to a significant reduction in LD number (p<0.001) compared to controls,

467   whereas NBAS silencing led to both a significant reduction in LD number and a

468   significant increase in LD size (p<0.001 in each case). The effects of SEC22A

469   silencing mirrored those of NBAS silencing, producing a significant reduction in LD

470   number (p<0.001) and a significant increase in LD size (p<0.001). Together, these

471   data implicate SEC22A in RAB18-mediated LD regulation.

472

473   <u>RAB18 recruits the orphan lipase TMCO4 to the ER membrane in a RAB3GAP-</u>

474   <u>dependent manner</u>

475   Among the lipid modifying/mobilizing proteins identified as potential RAB18 effectors

476   in HeLa cells, TMCO4 was identified in all three replicate experiments and its

477   association with RAB18 was highly RAB3GAP-dependent (association ratio 0.06).

478   TMCO4 (<u>t</u>rans<u>m</u>embrane and <u>co</u>iled-coil domains <u>4</u>) is annotated as containing

479   transmembrane and coiled-coil domains, but is orthologous to the Yeast protein Mil1/

480   Yfl034w. Mil1 was found to be peripherally membrane-associated/soluble, and is

481   thought to be an α/β hydrolase and a probable lipase based on structural modelling

482   (Whitfield et al., 2016). Consistent with this, a catalytic triad within its predicted active

483   site was shown to be required to confer tolerance to the membrane-intercalating

484   cationic amphipathic drug sertraline (Whitfield et al., 2016). The best template match

485   produced for TMCO4 by the structural modelling tool Phyre2 (Kelley et al., 2015) is

486   an acylglycerol/diacyclglycerol lipase (Figure S6). To explore the localization of

487   TMCO4, we expressed TMCO4-EGFP in HeLa cells (Figure 6). This construct

488   showed a diffuse appearance consistent with a largely cytosolic localization. In

489   contrast, EGFP-RAB18 partly localizes to the ER, as shown by its colocalization with

490   an ER marker (Figure 6A).

491   To assess the potential interaction between RAB18 and TMCO4, we coexpressed

492   mCherry-RAB18 and TMCO4-EGFP (Figure 6B). As in our previous experiments, we

493   used Celltrace reagents to distinguish cells of wild-type and mutant genotypes and

494   imaged these on the same dishes. In wild-type HeLa cells, we found that the

495   coexpression of mCherry-RAB18 led to a dramatic redistribution of TMCO4-EGFP to

496   the ER membrane suggesting that RAB18 is involved in the recruitment of TMCO4 to

497   this compartment (Figure 6B, upper panels). This redistribution was completely

498   absent in RAB3GAP1- and RAB3GAP2-null cells but unaffected in TRAPPC9-null

499   cells consistent with the BioID data. As a means of verifying the interaction, we

500   carried out immunoprecipitation experiments using exogenous HA-RAB18 and

501   TMCO4-EGFP (Figure 6C). As expected, TMCO4-EGFP copurified with HA-RAB18

502   when expressed in wild-type or TRAPPC9-null cells, but not when expressed in

503   RAB3GAP1-null cells. These data indicate that RAB18 and TMCO4 interact directly

504   or indirectly as part of a protein complex in a RAB3GAP-dependent manner. Further,

505   both the microscopy and the immunoprecipitation data support the suggestion that

506   different GEFs can promote different RAB18-interactions.

507

508   <u>RAB18 is involved in the mobilization of cholesterol</u>

509   The lipid-related RAB3GAP-dependent RAB18-associated proteins in the HeLa

510   BioID dataset included EBP, which is involved in cholesterol biosynthesis (Silve et

511   al., 1996). ORP2/OSBPL2 and INPP5B are also robustly linked to cholesterol,

512   functioning in cholesterol mobilization. ORP2 is thought to function as a lipid transfer

513   protein that delivers cholesterol to the plasma membrane (PM) in exchange for

514   PI(4,5)P$_2$, whereas INPP5B is implicated in the hydrolysis of ORP2-bound PI(4,5)P$_2$,

515   presumably driving the exchange process (Wang et al., 2019). Two other proteins in

516   this group, C2CD2L/TMEM24 and C2CD2, have not been linked to cholesterol, but

517   C2CD2L is characterised as a PI transporter and found to promote PM PI(4,5)P$_2$

518   synthesis (Lees et al., 2017). Limited information is available about the function of

519   *TMCO4* in mammals. However, it was identified in one study as one of a number of

520   genes with upregulated expression in rabbit cerebral arteries under conditions of

521   hypercholesterolemia (Ong et al., 2013). Another study suggests that TMCO4 is

522   present on lipid rafts (Jin et al., 2012). On the basis of these combined findings, we

523   investigated the potential role of RAB18 in cholesterol uptake and efflux.

524   We performed loading and efflux experiments to demonstrate the flux of

525   cholesterol/cholesteryl ester (CE) based on the activity of RAB18. Chinese hamster

526   ovary (CHO) cells were generated to stably express RAB18(WT), RAB18(Gln67Leu),

527   or RAB18(Ser22Asn). These cells were then preincubated with lipoprotein deficient

528   serum (LPDS) before addition of [^{14}C]-oleate for 24 hours. [^{14}C]-oleate was added in

529   the presence of LPDS (Figure 7A, left panel) or 10% FBS (Figure 7A, right panel).

530   [^{14}C]-CE levels were measured at t=0, and efflux was assessed by measuring CE

531   levels 4 and 8 hours following the addition of high density lipoprotein (HDL) to the

532   cells. In each case, [^{14}C]-CE was isolated by thin layer chromatography quantified by

533   scintillation counting. Efflux was also assessed directly by loading the cells with [^{3}H]-

534   cholesterol, then incubating them with apolipoprotein (apo) A-I. [^{3}H]-cholesterol

535   associated with apoA-I in the medium, as a percentage of total cellular radioactivity,

536   is shown in Figure 7B.

537   In cells loaded with [^{14}C]-oleate/LPDS, levels of CE were comparable in

538   RAB18(Ser22Asn) and RAB18(WT) cells, whereas RAB18(Gln67Leu) cells stored

539   significantly more (Figure 7A, left panel). In cells loaded with [^{14}C]-oleate/FBS, levels

540   of CE in RAB18(Ser22Asn) remained unchanged, whereas storage its storage was

541   elevated in RAB18(WT) cells and RAB18(Gln67Leu) cells (Figure 7A, right panel).

542   Interestingly, in both [^{14}C]-oleate/LPDS-loaded and [^{14}C]-oleate/FBS-loaded cells,

543   the addition of HDL led to rapid depletion of CE in RAB18(Gln67Leu) cells, but not in

544   RAB18(Ser22Asn) or RAB18(WT) cells (Figure 7A). Consistently, [^{3}H]-cholesterol

545   also underwent significantly more rapid efflux from these cells (Figure 7B).

546   Collectively, these data indicate that 'activated' GTP-bound RAB18 strongly

547   promotes the turnover and mobilization of CE.

548

549   DISCUSSION

550

551   In this study, we have complemented previous work showing that proximity

552   biotinylation is a powerful means of identifying candidate Rab effectors (Gillingham

553   et al., 2019). We have shown that comparisons between wild-type and nucleotide-

554   binding deficient BirA*-RAB18 fusions can help to distinguish putative effector

555   proteins, recapitulating findings from conventional affinity purification. Further, we

556   have found that comparing biotin-labelling produced by a BirA*-Rab in wild-type and

557   GEF-deficient cells can be particularly informative. For RAB18, we found that the

558   disruption of different GEF complexes affected largely distinct subsets of its

559   associations. Encouragingly, in the case of RAB3GAP-null cells, we found that

560   marked changes in RAB18-associations were restricted to a relatively small number

561   of proteins and that these comprised known and/or plausible interactors. By

562   identifying these, we were able to exclude ~95% of RAB18-associations from

563   consideration as more likely to represent 'noise' from bystander proteins.

564   The limited overlap between RAB3GAP- and TRAPPC9-dependent RAB18

565   associations is interesting because it may indicate that different RAB18-GEFs control

566   different aspects of RAB18 function. However, the large number of RAB18-

567   associations affected in TRAPPC9-null cells may not all represent functional

568   interactions. Loss of TRAPPC9 does not appear to affect RAB18 localization (Figure

569   S2C). Nevertheless, it could affect RAB18-associations indirectly. TRAPP complexes

570   regulate multiple Rab isoforms, and so broad disruption of membrane trafficking

571   might alter the compliment of RAB18-proximal proteins. Nevertheless, it seems likely

572   that genuine TRAPPII-dependent RAB18-associations are represented in our

573   dataset.

574   For validation of our BioID screening, we focused on the subset of RAB3GAP-

575   dependent candidate RAB18 effectors. These 25 proteins largely fell into three

576   apparently interrelated functional groups: microtubule-interacting/membrane-

577   remodelling proteins; proteins involved in bringing membranes into close apposition;

578   and proteins involved in lipid modification and mobilization. It has been proposed that

579   RAB18 functions to coordinate lipid transfer between apposed membranes, and our

580   data are consistent with this model (Xu et al., 2018). Though not definitively

581 demonstrated in the present study, it seems likely that membrane remodelling

582 precedes the engagement of tethers and SNAREs and the establishment of

583 membrane-contacts. Lipid transporter/exchange proteins are required for lipid

584 transfer to occur at these contact points, while lipid-modifying proteins may serve to

585 generate concentration gradients necessary to promote directional flow. We have

586 presented preliminary findings supporting functional interactions between RAB18

587 and one protein from each group; two of these interactors, SEC22A and TMCO4,

588 had not been reported previously.

589 In initial screening of 12 of the candidate effectors by IF, we observed that levels of

590 SPG20 were reduced in the absence of RAB18 or TBC1D20 in two different cell

591 types. SPG20 is a protein of enigmatic function, having been ascribed roles in

592 regulating microtubule stability and bone morphogenic protein (BMP) signalling,

593 chromosome segregation and cytokinesis, LD turnover and ubiquitylation of LD

594 proteins, and in mitochondrial energy metabolism and calcium homeostasis

595 (Eastman et al., 2009, Edwards et al., 2009, Joshi and Bakowska, 2011, Lind et al.,

596 2011, Nahm et al., 2013, Nicholson et al., 2015, Renvoise et al., 2012, Ring et al.,

597 2017, Tsang et al., 2009). Of particular interest in the context of RAB18 and its

598 association with Warburg Micro syndrome, biallelic loss-of-function variants in

599 *SPG20* cause Troyer syndrome, which has overlapping features including ID and

600 ascending paraplegia (Baple and Crosby, 1993). One possible avenue for future

601 research could be the potential relationship between SPG20 and the other RAB18-

602 associated microtubule (MT)-binding proteins identified in this study. Like SPG20,

603 CAMSAP1 is found to associate with poles of the mitotic spindle (Hueschen et al.,

604 2017, Lind et al., 2011). CAMSAP1 is a MT minus-end binding protein whereas

605 BICD2 is a component of a minus-end-directed dynein-dynactin motor complex

606 (Hendershott and Vale, 2014, Hueschen et al., 2017, Urnavicius et al., 2015).

607 REEP4 is localized to the ER, and like RAB18 is linked to the regulation of ER

608 structure (Kumar et al., 2019, Gerondopoulos et al., 2014). However, it also

609 contributes to the clearance of ER from metaphase chromatin (Schlaitz et al., 2013).

610 This role is dependent on its MT-binding, and therefore spindle-binding during

611 metaphase. Thus, these four MT-binding proteins all function in the same

612 spatiotemporally defined compartment during mitosis.

613   Among the membrane tethering and docking proteins associated with RAB18, we

614   investigated SEC22A on the basis of its homology to SEC22B. SEC22B is a

615   component of the canonical syntaxin 18 SNARE complex, and other components of

616   this complex interact with RAB18 to regulate close apposition of membranes, though

617   SEC22B itself is not necessary for this activity (Xu et al., 2018). Reciprocal proximity

618   biotinylation with a BioID2-SEC22A fusion was consistent with a RAB3GAP-

619   dependent RAB18-SEC22A interaction, and suggested that other SEC22A

620   interactions are altered when RAB18 is absent or dysregulated. We also found that

621   the silencing of SEC22A led to altered LD morphology, similar to that previously

622   observed when expression of other RAB18-associated tethering/docking proteins

623   was disrupted. It is tempting to speculate that SEC22A contributes to a non-

624   fusogenic SNARE complex, since it lacks the SNARE domain usually required to

625   provide the mechanical force for fusion. SNARE proteins can be relatively

626   promiscuous in their interactions, and there are numerous examples of individual

627   SNAREs contributing to distinct SNARE complexes (Wang et al., 2017, Petkovic et

628   al., 2014). There are also examples in which SNARE complexes mediate the stable

629   association of membranes rather than their fusion (Petkovic et al., 2014).

630   Rab proteins, SM proteins and tethering factors can contribute to compartmental

631   specificity and the assembly of specific SNARE complexes. In Yeast, the RAB1

632   orthologue Ypt1p and the SM protein Sly1p are implicated in the assembly of the

633   canonical syntaxin 18 (Ufe1p) SNARE complex (Kamena et al., 2008, Yamaguchi et

634   al., 2002, Dilcher et al., 2003, Lewis and Pelham, 1996, Lewis et al., 1997). In

635   mammals, multiple Rab isoform(s) and the Sly1p orthologue SCFD1 may fulfil this

636   role (Nakajima et al., 2004, Hirose et al., 2004, Galea et al., 2015, Tagaya et al.,

637   2014). The suggestion that RAB18 regulates assembly of a distinct SNARE complex

638   (Xu et al., 2018) is consistent both with our identification of SEC22A as a RAB18-

639   associated protein, and also with our finding that SCFD2 but not SCFD1 associates

640   with RAB18 in a RAB3GAP-dependent manner. SCFD2 is a poorly characterised

641   Sly1p orthologue, but dramatic effects of SCFD1 silencing on the secretory pathway

642   suggest that SCFD1 and SCFD2 do not function redundantly (Bassaganyas et al.,

643   2019). Although we did not validate the RAB18-SCFD2 association directly, it has

644   recently been reported in another study (Gillingham et al., 2019).

645   The lipid modifying/mobilizing proteins that we found associated with RAB18

646   included the poorly characterised orphan lipase TMCO4. We have presented clear

647   evidence for the RAB3GAP-dependent recruitment of TMCO4 to the ER by RAB18,

648   further validating the BioID approach and dataset. We have not yet conclusively

649   proven the link between RAB18 and the other lipid-related proteins in this group,

650   ORP2, INPP5B, C2CD2, C2CD2L and EBP. Any conjecture based on these

651   prospective interactions therefore remains tentative. Nevertheless, we have shown

652   that RAB18 influences cellular cholesterol mobilization, a process in which TMCO4

653   may be involved, and in which ORP2 and INPP5B appear to have a central role

654   (Lees et al., 2017). ORP2 is thought to act as cholesterol-PI(4,5)P_2 exchanger,

655   whereas INPP5B is thought to drive the exchange process by catalysing PI(4,5)P_2

656   hydrolysis. Therefore, these proteins are strong candidates for future investigation.

657   Interestingly, INPP5B has been shown in several studies to have a relatively broad

658   Rab-binding specificity (Fukuda et al., 2008, Williams et al., 2007). Further, many

659   other phosphoinositide phosphatase enzymes, including members from distinct

660   protein families, bind to Rab proteins (Gillingham et al., 2019). Multiple OSBP-

661   homologues also bind to Rabs (Gillingham et al., 2019, Rocha et al., 2009, Sobajima

662   et al., 2018), raising the possibility that phosphoinositide-unloading from OSBPs

663   constitutes a conserved role for RAB proteins generally: different Rab isoforms may

664   specify intermembrane transfer of different lipid species by association with different

665   combinations of phosphatase and OSBP proteins. One interesting possibility we are

666   currently pursuing is that RAB18 may contribute to cholesterol biosynthesis though

667   the delivery of substrate to the EBP enzyme, or through the relocalization of the lipid

668   species it generates.

669   To summarise, we have used complementary proximity ligation approaches together

670   with CRISPR gene-editing to inventory RAB18-associated proteins. The RAB3GAP-

671   dependent RAB18-associations we have highlighted are supported by additional

672   validation of three examples, as well as by correlative information from the literature.

673   Broadly, the latter suggests a role for Rab proteins distinct from that in mediating

674   vesicular membrane traffic. Another role of Rabs may be to assemble a network of

675   diverse membrane-membrane contact sites and then orchestrate highly regulated

676   metabolism and flow of lipid species within a discontinuous lipid phase. We have

677   shown that RAB18 influences cholesterol mobilization, and priorities for future work

678   will be to categorically define the molecular mechanism involved and to determine

679   whether altered cholesterol flux underlies the pathology of Warburg Micro syndrome.

680   Since several of the putative RAB18 effectors we have uncovered are also encoded

681   by disease-associated genes, a further aim will be to determine the extent to which

682   the molecular pathology of these conditions overlap.

683

684

685

686   MATERIALS AND METHODS

687

688   <u>Plasmids</u>

689   Generation of recombinant pcDNA5 FRT/TO FLAG-BirA(Arg118Gly) vectors for

690   preparation of stable T-Rex-293 cell lines is described below. Generation of

691   recombinant pX461 and pX462 plasmids for CRISPR gene-editing is described

692   below. Generation of recombinant pCMV vectors for preparation of stable CHO cell

693   lines is described below. The EGFP-RAB18 construct has been described previously

694   (Gerondopoulos et al., 2014). The RAB18 sequence was excised from this construct

695   using BamHI and HindIII restriction enzymes (New England Biolabs, Hitchin, UK),

696   and used to generate constructs encoding mEmerald-RAB18 and mCherry-RAB18

697   by ligation into mEmerald-C1 and mCherry-C1 vectors (Addgene, Watertown, MA)

698   using HC T4 Ligase and rapid ligation buffer (Promega, Southampton, UK).

699   Constructs encoding BirA*-RAB18, BioID2(Gly40Ser)-SEC22A, mEmerald-SEC22A,

700   mEmerald-SPG20 and mEmerald-RAB7A were generated following PCR

701   amplification from template and subcloning into an intermediate pCR-Blunt II-TOPO

702   vector using a Zero Blunt TOPO PCR Cloning Kit (ThermoFisher Scientific,

703   Waltham, MA) according to manufacturer's instructions. Fragments were excised

704   from intermediate vectors and then subcloned into target vectors using restriction-

705   ligation, as above. A construct encoding mCherry-ER was obtained from Addgene,

706   and a construct encoding TMCO4-EGFP was synthesised and cloned by GeneWiz

707   (Leipzig, Germany). Details of PCR templates, primers and target vectors are listed

708   in Table S6.

709

710   <u>Antibodies and reagents</u>

711   A custom polyclonal antibody to RAB18 generated by Eurogentec (Southampton,

712   UK) has been described previously (Handley et al., 2015). An antibody to

713   RAB3GAP1 was obtained from Bethyl Labs (Montgomery, TX), an antibody to GFP

714   was obtained from Takara Bio (Saint-Germain-en-Laye, France), an antibody to β-

715   Tubulin was obtained from Abcam (Cambridge, UK) and an antibody to β-Actin was

716   obtained from ThermoFisher. Antibodies to hemagglutinin (HA), RAB3GAP2 and

717   TBC1D20 were obtained from Merck (Gillingham, UK). Antibodies to ZW10, STX18,

718   SPG20, RINT1, REEP4, BNIP1, C2CD2, TRIM13, WFS1, INPP5B, OSBPL2 and

719   NBAS were obtained from Proteintech (Manchester, UK). Antibody catalogue

720   numbers and the dilutions used in this study are listed in Table S6.

721

722   <u>Cell culture</u>

723   T-REx-293,HeLa and IHH cells were maintained in DMEM media, RPE1 cells in

724   DMEM/F12 media and CHO cells in alpha-MEM media (ThermoFisher). In each

725   case, media was supplemented with 10% foetal calf serum (FCS) and 1% penicillin-

726   streptomycin (PS). Cells were maintained at 37°C and 5% CO_2.

727

728   <u>Generation of stable T-Rex-293 and CHO cell lines</u>

729   PCR products encoding mouse RAB18, RAB18(Gln67Leu) and RAB18(Ser22Asn)

730   were subcloned into NotI-linearized pcDNA5 FRT/TO FLAG-BirA(Arg118Gly) vector

731   using the In-Fusion HD EcoDry Cloning Plus kit (Takara Bio) according to

732   manufacturer's instructions. Details of PCR templates, primers and target vectors are

733   listed in Table S6. 1.5ug of each recombinant vector together with 13.5ug of pOG44

734   plasmid (ThermoFisher) were used in cotransfections of T-REx-293 cells, in 10cm

735   dishes, with TransIT-LT1 Transfection Reagent (Mirus Bio, Madison, WI).16 hours

736   following transfection, media was replaced and cells were allowed to recover for 24

737   hours. Each dish was then split to 4x 10cm dishes in selection media containing 10

738   ug/ml Blasticidin and 50 ug/ml Hygromycin B. Resistant clones were pooled and

739   passaged once prior to use.

740   A PCR product encoding mouse RAB18 was subcloned into an intermediate TOPO

741   vector using a TOPO PCR Cloning Kit (ThermoFisher) according to manufacturer's

742   instructions. The RAB18 fragment was then excised and subcloned into the pCMV

743   vector. PCR-based site-directed mutagenesis using a GeneArt kit (ThermoFisher)

744   was then used to generate pCMV-RAB18(Gln67Leu) and pCMV-RAB18(Ser22Asn)

745   constructs. CHO cells were transfected using Lipofectamine 2000 reagent

746   (ThermoFisher) and cells stably-expressing each construct were selected-for with

747   blasticidin. Under continued selection, clonal cell-lines were grown from single cells

748   and then RAB18 protein expression was assessed. Cell lines comparably expressing

749   RAB18 constructs at levels 2.5-5x higher than those wild-type cells were used in

750   subsequent experiments.

751

752   Generation of clonal 'knockout' HeLa and RPE1 cell lines

753   CRISPR/Cas9 gene-editing was carried out essentially as described in Ran et al.,

754   2013 (Ran et al., 2013). Guide RNA (gRNA) sequences are shown in (Table S6). A

755   list of the clonal cell lines generated for this study, together with the loss-of-function

756   variants they carry is shown in (Figure S1A). Western blot validation is shown in

757   (Figure S1B-E). Briefly, for each targeted exon, pairs of gRNA sequences were

758   selected using the online CRISPR design tool (http://crispr.mit.edu/). Oligonucleotide

759   pairs incorporating these sequences (Sigma) were annealed (at 50mM ea.) in 10mM

760   Tris pH8, 50mM NaCl and 1mM EDTA by incubation at 95ºC for 10 minutes followed

761   by cooling to room temperature. Annealed oligonucleotides were diluted and ligated

762   into BbsI-digested pX461 and pX462 plasmids (Addgene) using HC T4 Ligase and

763   rapid ligation buffer (Promega). Sequences of all recombinant plasmids were verified

764   by direct sequencing. Pairs of plasmids were contransfected into cells using

765   Lipofectamine 2000 reagent according to manufacturer's instructions. Cells were

766   selected for puromycin resistance (conferred by pX462) using 24 hours puromycin-

767   treatment. Following 12 hours recovery, they were selected for GFP fluorescence

768   (conferred by pX461) and cloned using FACSAria2 SORP, Influx or FACSMelody

769   instruments (BD, Wokingham, UK). After sufficient growth, clones were analysed by

770   PCR of the targeted exons (Primers are listed in Table S6). In order to sequence

771   individual gene edited-alleles, PCR products from each clone were first cloned into

772   ZeroBlunt TOPO vector (ThermoFisher) and then subjected to colony PCR. These

773   PCR products were then analysed by direct sequencing. Sequencing data was

774   assessed using BioEdit software (http://www.mbio.ncsu.edu/BioEdit/bioedit.html).

775

776   BirA/BioID proximity labelling (T-REx-293 cells)

777   The T-REx-293 Cell Lines (described above) were seeded onto 3x 15cm plates each

778   and allowed to adhere. Expression of BirA*-RAB18 fusion proteins was induced by

779   treatment with 20ng/ml Tetracycline for 16 hours. Media was then replaced with

780   media containing 20% FBS, 20 ng/ml Tetracycline and 50 uM Biotin and the cells

781   were incubated for a further 8 hours, washed with warmed PBS and pelleted in ice-

782   cold PBS. Cell pellets were snap-frozen and stored at -80ºC prior to lysis. Lysis was

783   carried out in 3ml of ice-cold RIPA buffer (150 mM NaCl, 1% NP40, 0.5% Sodium

784   Deoxycholate, 0.1% SDS, 1mM EDTA, 50mM Tris, pH 7.4) supplemented with

785   complete-mini protease inhibitor cocktail (Roche, Basel, Switzerland), 1mM PMSF,

786   and 62.5 U/ml Benzonase (Merck). Lysates were incubated for 1 hour at 4ºC then

787   sonicated in an ice bath (four 10 second bursts on low power). They were then

788   clarified by centrifugation, and the supernatants transferred to tubes containing pre-

789   washed streptavidin-sepharose (30µl bed-volume)(Merck). The beads were

790   incubated for 3 hours at 4ºC, then washed x5 in RIPA buffer and x4 in buffer

791   containing 100mM NaCl, 0.025% SDS and 25 mM Tris, pH7.4.

792

793   <u>BirA*/BioID proximity labelling (HeLa cells)</u>

794   Proximity-labelling in HeLa cells was carried out largely as described by Roux et al.

795   (Roux et al., 2012), but with minor modifications. HeLa cells were grown to 80%

796   confluence in T75 flasks and then each flask was transfected with 1-1.5µg of the

797   BirA*-RAB18 construct or 1µg of the BioID2(Gly40Ser)-SEC22A construct using

798   Lipofectamine 2000 reagent in Optimem serum-free medium (ThermoFisher) for 4

799   hours, according to manufacturer's instructions. 24 hours post-transfection, media

800   was replaced with fresh media containing 50µM Biotin (Merck) and the cells were

801   incubated for a further 24 or 6 hours (for BirA*-RAB18 and BioID2(Gly40Ser)-

802   SEC22A experiments respectively). Cells were then trypsinised and washed twice in

803   PBS before pellets were transferred to 2ml microcentrifuge tubes and snap-frozen.

804   For each pellet, lysis was carried out in 420µl of a buffer containing 0.2% SDS, 6%

805   Triton-X-100, 500mM NaCl, 1mM DTT, EDTA-free protease-inhibitor solution

806   (Expedeon, Cambridge, UK), 50mM Tris pH7.4. Lysates were sonicated for 10

807   minutes using a Bioruptor device together with protein extraction beads (Diagenode,

808   Denville, NJ). Each lysate was diluted with 1080µl 50mM Tris pH7.4, and they were

809   then clarified by centrifugation at 20 000xg for 30 minutes at 4ºC. Affinity purification

810   of biotinylated proteins was carried out by incubation of clarified lysates with

811   streptavidin-coated magnetic Dynabeads (ThermoFisher) for 24 hours at 4ºC. Note

812   that a mixture of Dynabeads - MyOne C1, MyOne T1, M270 and M280 – was used

813   to overcome a problem with bead-clumping observed when MyOne C1 beads were

814   used alone. Successive washes were carried out at room temperature with 2% SDS,

815   a buffer containing 1% Triton-X-100, 1mM EDTA, 500mM NaCl, 50mM HEPES

816   pH7.5, a buffer containing 0.5% NP40, 1mM EDTA, 250mM LiCl, 10mM Tris pH7.4,

817   50mM Tris pH7.4 and 50mM ammonium bicarbonate.

818

819   <u>Preparation of cell lysates for label-free quantitative proteomics</u>

820   RPE1 and HeLa cells were grown to confluence in T75 flasks. They were then

821   trypsinised, and cell pellets were washed with PBS and snap-frozen prior to use.

822   RPE1 pellets were resuspended in 300µl 6M GnHCl, 75mM Tris, pH=8.5. HeLa

823   pellets were resuspended in 300µl 8M urea, 75mM NaCl, 50mM Tris, pH=8.4. In

824   each case, samples were sonicated for 10 minutes using a Bioruptor device together

825   with protein extraction beads (Diagenode). RPE1 samples were heated for 5 minutes

826   at 95ºC. Samples were clarified by centrifugation.

827

828   <u>Mass spectrometry</u>

829   Washed beads from BioID experiments with T-Rex-293 cell lines were resuspended

830   in 50µl 6M urea, 2M thiourea, 10mM Tris, pH=8.5 and DTT was added to 1mM. After

831   30 minutes incubation at 37ºC, samples were alkylated with 5mM iodoacetamide

832   (IAA) in the dark for 20minutes. DTT was increased to 5mM and 1µg lysC was

833   added, then samples were incubated at 37ºC for 6 hours. Samples were diluted to

834   1.4M urea, then digested with trypsin (Promega), overnight at 37°C, according to

835   manufacturer's instructions. Samples were acidified by the addition of 0.9% formic

836   acid and 5% acetonitrile.

837   Washed beads from BioID experiments with HeLa cells were subjected to limited

838   proteolysis by trypsin (0.3 ug) at 27°C for 6.5hours in 2mM urea, 1mM DTT, 75mM

839   Tris, pH=8.5, then supernatants were incubated overnight at 37°C. Samples were

840   alkylated with 50mM IAA in the dark for 20minutes, then acidified by addition of 8µl

841   10% trifluoroacetic acid (TFA). RPE1 lysates were reduced and alkylated through

842   addition of tris(2-carboxyethyl)phosphine (TCEP) and 2-chloroacetamide (CAA) to

843   5mM and 10mM respectively and then incubated at 95°C for 5 minutes. After

844   cooling, samples were diluted to 3M guanidine and 0.5µg lysC added with incubation

845   overnight at 37°C. A further dilution to 1M guanidine was followed by digest with

846   0.3µg trypsin at 37°C for 4 hours. Samples were acidified with TFA. HeLa lysates

847   were reduced and alkylated by addition of DTT to 10mM, then by addition of IAA to

848   25mM, then further addition of DTT to 25mM, with incubation at room temperature

849   for 30-60 minutes following each step. Samples were digested with lysC, overnight at

850   37°C. They were then diluted to 2M urea, and further digested, overnight at 37°C.

851   Samples were acidified with TFA.

852   For BioID samples from T-REx-293 cells, LC-MS was carried out as previously

853   described (Brunet et al., 2016). Briefly, peptides in an aqueous solution containing

854   5% acetonitrile and 0.1% formic acid were loaded onto a 3 µm PepMap100, 2 cm, 75

855   µm diameter sample column using an Easy nLC 1000 ultrahigh pressure liquid

856   chromatography system (ThermoFisher). They were eluted with acetonitrile/formic

857   acid into an in-line 50 cm separating column (2 µm PepMap C18, 75 µm diameter) at

858   40°C. Separated peptides were ionized using an Easy Spray nano source and

859   subjected to MS/MS analysis using a Velos Orbitrap instrument (ThermoFisher).

860   Following acquisition, data were analysed using SEAQUEST software.

861   For other samples, peptides were loaded on to activated (methanol), equilibrated

862   (0.1% TFA) C18 stage tips before being washed with 0.1% TFA and eluted with

863   0.1% TFA/80 acetonitrile. The organic was dried off, 0.1% TFA added to 15 µl and 5

864   µl injected onto LC-MS. Peptides were separated on an Ultimate nano HPLC

865   instrument (ThermoFisher), and analysed on either an Orbitrap Lumos or a Q

866   Exactive Plus instrument (ThermoFisher). After data-dependent acquisition of HCD

867   fragmentation spectra, data were analysed using MaxQuant and the uniprot human

868   reference proteome. Versions, releases, parameters and gradients used for

869   separation are provided in table S6.

870

871   Cell labelling

872   In order to distinguish cells of different genotypes within the same well/on the same

873   coverslip, CellTrace Violet and CellTrace Far Red reagents (ThermoFisher) were

874   used to label cells before they were seeded. Cells of different genotypes were first

875   trypsinised and washed with PBS separately. They were then stained in suspension

876   by incubation with either 1μM CellTrace Violet or 200nM CellTrace Far Red for 20

877   minutes at 37°C. Remaining dye was removed by addition of a ten-fold excess of full

878   media, incubation for a further 5 minutes, and then by centrifugation and

879   resuspension of the resulting pellets in fresh media. Differently-labelled cells were

880   combined prior to seeding.

881

882   <u>Immunofluorescence microscopy</u>

883   HeLa or RPE1 cells were seeded in 96-well glass-bottom plates (PerkinElmer,

884   Waltham, MA) coated with Matrigel (Corning, Amsterdam, Netherlands) according to

885   manufacturer's instructions, and allowed to adhere for 48 hours prior to fixation. In

886   lipid-loading experiments, cells were treated with 200μM oleic acid complexed to

887   albumin (Merck) and 1μg/ml BODIPY-558/568-C12 (ThermoFisher) for 15 hours

888   prior to fixation. Cells were fixed using a solution of 3% deionised Glyoxal, 20%

889   EtOH, 0.75% acetic acid, pH=5 (Richter et al., 2018), for 20 minutes at room

890   temperature. They were then washed with PBS containing 0.9mM $CaCl_2$ and 0.5mM

891    $MgCl_2$ and blocked with a sterile-filtered buffer containing 1% Milk, 2% donkey serum

892   (Merck), 0.05% Triton-X-100 (Merck), 0.9mM $CaCl_2$ and 0.5mM $MgCl_2$ in PBS

893   pH=7.4 for at least 1 hour prior to incubation with primary antibody. Primary

894   antibodies were added in blocking buffer without Triton-X-100, and plates were

895   incubated overnight at 4ºC. Antibody dilutions are listed in Table S6. Following

896   washing in PBS, cells were incubated with 1:2000 Alexa 488-conjugated secondary

897   antibody (ThermoFisher) in blocking buffer at room temperature for 1-2 hours.

898   Following further washing in PBS, cells were imaged using an Operetta High Content

899   Imaging System (PerkinElmer) equipped with Harmony software. In comparative

900   fluorescence quantitation experiments, at least 18 frames – each containing >5 wild-

901   type and >5 mutant cells – were analysed per genotype. ImageJ software was used

902   to produce regions of interest (ROIs) corresponding to each cell using thresholding

903   tools and images from the 405nm and 645nm channels. Median 490nm fluorescence

904   intensity was measured for each cell and mutant fluorescence intensity (as %wild-

905   type) was calculated for each frame and combined for each genotype.

906

907   <u>Confocal microscopy – Live cell imaging</u>

908 HeLa or RPE1 cells were seeded on glass-bottom dishes (World Precision
909 Instruments, Hitchin, UK) coated with Matrigel (Corning) and allowed to adhere for
910 24 hours prior to transfection. Transfections and cotransfections were carried out
911 with 0.5µg of each of the indicated constructs using Lipofectamine 2000 reagent in
912 Optimem serum-free medium for 4 hours, according to manufacturer's instructions.
913 Media were replaced and cells were allowed to recover for at least 18 hours prior to
914 imaging. Imaging was carried out on a Nikon A1R confocal microscope equipped
915 with the Nikon Perfect Focus System using a 60× oil immersion objective with a 1.4
916 numerical aperture. In immunofluorescence experiments, the pinhole was set to
917 airy1. CellTrace Violet was excited using a 403.5nm laser, and emitted light was
918 collected at 425–475nm. EGFP and mEmerald were excited using a 488 nm laser,
919 and emitted light was collected at 500–550 nm. BODIPY-558/568-C12 and mCherry
920 were excited using a 561.3 nm laser, and emitted light was collected at 570–620 nm.
921 CellTrace Far Red was excited using a 638nm laser, and emitted light was collected
922 at 663-738nm. In fluorescence recovery after photobleaching (FRAP) experiments,
923 the pinhole was set to airy2 and digital zoom parameters were kept constant.
924 Bleaching was carried out using 90% laser power.

925

926 Immunoprecipitation

927 HeLa cells were seeded onto 10cm dishes and allowed to adhere for 24 hours prior
928 to transfection. Transfections and cotransfections were carried out with 0.5µg of
929 each of the indicated constructs using Lipofectamine 2000 reagent in Optimem
930 serum-free medium for 4 hours, according to manufacturer's instructions. 24 hours
931 post-transfection cells were trypsinised, washed with PBS, then lysed in a buffer
932 containing 150mM NaCl, 0.5% Triton-X-100 and EDTA-free protease-inhibitor
933 solution (Expedeon), 10mM Tris, pH=7.4. Lysates were clarified by centrifugation,
934 input samples taken, and the remaining supernatants then added to 4µg rabbit anti-
935 HA antibody (Merck). After 30 minutes incubation at 4ºC on a rotator, 100µl washed
936 protein G-coupled Dynabeads (ThermoFisher) were added and samples were
937 incubated for a further 1 hour. The Dynabeads were washed x3 with buffer
938 containing 150mM NaCl, 0.1% Triton-X-100, 10mM Tris, pH=7.4, then combined with
939 a reducing loading buffer and subjected to SDS–PAGE.

940   <u>Lipid loading experiments</u>

941   For LD number and diameter measurements, IHH cells were seeded onto glass

942   coverslips. siRNA transfections were carried out using FuGene reagent (Promega)

943   according to manufacturer's instructions. siRNAs targeting ZW10 and NBAS were

944   obtained from IDT, Coralville, IA; siRNA targeting SEC22A was obtained from

945   Horizon Discovery, Cambridge, UK. 48 hours following transfection, cells were

946   treated with 200nM BSA conjugated oleate for 24 hours. Coverslips were washed,

947   fixed with 3% paraformaldehyde and stained with 1ug/mL BODIPY and 300nM DAPI.

948   Fluorescence images were captured on a Zeiss LSM 780 confocal microscope

949   equipped with a 100x objective. Images were analysed using ImageJ software. Data

950   are derived from measurements from >100 cells/condition and are representative of

951   three independent experiments.

952   For cholesterol storage and efflux experiments with [^{14}C]-oleate, CHO cell lines

953   (described above) were seeded onto 12-well plates and then grown to 60-75%

954   confluence in Alpha media supplemented with 10% LPDS. Cells were grown in the

955   presence of 10% LPDS for at least 24 hours prior to the addition of oleate. 1 µCi/ml

956   [^{14}C]-oleate (Perkin Elmer) was added in the presence of 10% LPDS or 10% FBS for

957   24 hours. Cells were then washed and incubated with 50µg/ml HDL for 0, 4 or 8

958   hours. Cellular lipids were extracted with hexane. Lipids were then dried-down and

959   separated by thin layer chromatography (TLC) in a hexane:diethyl ether:acetic acid

960   (80:20:2) solvent system. TLC plates were obtained from Analtech, Newark, NJ.

961   Bands corresponding to cholesteryl ester (CE) were scraped from the TLC plate, and

962   radioactivity was determined by scintillation counting in a Beckman Coulter LS6500

963   Scintillation Counter using BetaMax ES Liquid Scintillation Cocktail (ThermoFisher).

964   Three independent experiments were carried out, each with four replicates of each

965   condition. Data from a representative experiment are shown.

966   For cholesterol efflux experiments with [^{3}H]-cholesterol, CHO cells were seeded onto

967   12-well plates and then grown to 60% confluence in Alpha media supplemented with

968   10% FBS. 5 µCi/ml [^{3}H]-cholesterol (PerkinElmer) was added in the presence of 10%

969   FBS. After 3x PBS washes, cells were incubated with serum-free media containing

970   25µg/ml of human apolipoprotein A-I (ApoA-I) for 5 hours. ApoA-I was a kind gift of

971   Dr. Paul Weers (California State University, Long Beach). Radioactivity in aliquots of

972 media were determined by scintillation counting in a Beckman Coulter LS6500

973 Scintillation Counter using LSC Cocktail (PerkinElmer). Cell lysates were produced

974 by addition of 0.1N NaOH for 1 hour, and their radioactivity was determined as

975 above. Cholesterol efflux was calculated as an average (+/- SD) of the % cholesterol

976 efflux (as a ratio of the media cpm/(media + cellular cpm) x 100%).

977 <u>Western blotting</u>

978 Cell lysates were made with a buffer containing 150mM NaCl, 0.5% Triton-X-100

979 and EDTA-free protease-inhibitor solution (Expedeon), 50mM Tris, pH=7.4. Cell

980 lysates and input samples from BioID and immunoprecipitation experiments were

981 combined 1:1 with a 2x reducing loading buffer; a reducing loading buffer containing

982 10mM EDTA was added directly to Dynabead samples. SDS–PAGE and Western

983 blotting were carried out according to standard methods.

984

985 ACKNOWLEDGEMENTS

988

989 COMPETING INTERESTS

990 No competing interests declared.

991

992 FUNDING

995

996 DATA AVAILABILITY

997 The mass spectrometry proteomics data have been deposited to the

998 ProteomeXchange Consortium via the PRIDE (Perez-Riverol et al., 2019) partner

999 repository with the dataset identifiers PXD016631, PXD016336, PXD016326,

1000 PXD016233 and PXD016404.

1001

1002

1003

1004

REFERENCES

Aligianis, I. A., Johnson, C. A., Gissen, P., Chen, D., Hampshire, D., Hoffmann, K., Maina, E. N., Morgan, N. V., Tee, L., Morton, J., Ainsworth, J. R., Horn, D., Rosser, E., Cole, T. R., Stolte-Dijkstra, I., Fieggen, K., Clayton-Smith, J., Megarbane, A., Shield, J. P., Newbury-Ecob, R., Dobyns, W. B., Graham, J. M., Jr., Kjaer, K. W., Warburg, M., Bond, J., Trembath, R. C., Harris, L. W., Takai, Y., Mundlos, S., Tannahill, D., Woods, C. G. & Maher, E. R. 2005. Mutations of the catalytic subunit of RAB3GAP cause Warburg Micro syndrome. *Nat Genet,* 37**,** 221-3.

Angebault, C., Fauconnier, J., Patergnani, S., Rieusset, J., Danese, A., Affortit, C. A., Jagodzinska, J., Megy, C., Quiles, M., Cazevieille, C., Korchagina, J., Bonnet-Wersinger, D., Milea, D., Hamel, C., Pinton, P., Thiry, M., Lacampagne, A., Delprat, B. & Delettre, C. 2018. ER-mitochondria cross-talk is regulated by the Ca(2+) sensor NCS1 and is impaired in Wolfram syndrome. *Sci Signal,* 11.

Baple, E. & Crosby, A. 1993. Troyer Syndrome. *In:* ADAM, M. P., ARDINGER, H. H., PAGON, R. A., WALLACE, S. E., BEAN, L. J. H., STEPHENS, K. & AMEMIYA, A. (eds.) *GeneReviews((R)).* Seattle (WA).

Barr, F. & Lambright, D. G. 2010. Rab GEFs and GAPs. *Curr Opin Cell Biol,* 22**,** 461-70.

Bassaganyas, L., Popa, S. J., Horlbeck, M., Puri, C., Stewart, S. E., Campelo, F., Ashok, A., Butnaru, C. M., Brouwers, N., Heydari, K., Ripoche, J., Weissman, J., Rubinsztein, D. C., Schekman, R., Malhotra, V., Moreau, K. & Villeneuve, J. 2019. New factors for protein transport identified by a genome-wide CRISPRi screen in mammalian cells. *J Cell Biol.*

Bekbulat, F., Schmitt, D., Feldmann, A., Huesmann, H., Eimer, S., Juretschke, T., Beli, P., Behl, C. & Kern, A. 2018. RAB18 impacts autophagy via lipid droplet-derived lipid transfer and is rescued by ATG9A. *bioRxiv***,** 421677.

Bem, D., Yoshimura, S., Nunes-Bastos, R., Bond, F. C., Kurian, M. A., Rahman, F., Handley, M. T., Hadzhiev, Y., Masood, I., Straatman-Iwanowska, A. A., Cullinane, A. R., Mcneill, A., Pasha, S. S., Kirby, G. A., Foster, K., Ahmed, Z., Morton, J. E., Williams, D., Graham, J. M., Dobyns, W. B., Burglen, L., Ainsworth, J. R., Gissen, P., Muller, F., Maher, E. R., Barr, F. A. & Aligianis, I. A. 2011. Loss-of-function mutations in RAB18 cause Warburg micro syndrome. *Am J Hum Genet,* 88**,** 499-507.

Borck, G., Wunram, H., Steiert, A., Volk, A. E., Korber, F., Roters, S., Herkenrath, P., Wollnik, B., Morris-Rosendahl, D. J. & Kubisch, C. 2011. A homozygous RAB3GAP2 mutation causes Warburg Micro syndrome. *Hum Genet,* 129**,** 45-50.

Branon, T. C., Bosch, J. A., Sanchez, A. D., Udeshi, N. D., Svinkina, T., Carr, S. A., Feldman, J. L., Perrimon, N. & Ting, A. Y. 2018. Efficient proximity labeling in living cells and organisms with TurboID. *Nat Biotechnol,* 36**,** 880-887.

Brunet, S., Saint-Dic, D., Milev, M. P., Nilsson, T. & Sacher, M. 2016. The TRAPP Subunit Trs130p Interacts with the GAP Gyp6p to Mediate Ypt6p Dynamics at the Late Golgi. *Front Cell Dev Biol,* 4**,** 48.

Bui, M., Gilady, S. Y., Fitzsimmons, R. E., Benson, M. D., Lynes, E. M., Gesson, K., Alto, N. M., Strack, S., Scott, J. D. & Simmen, T. 2010. Rab32 modulates apoptosis onset and mitochondria-associated membrane (MAM) properties. *J Biol Chem,* 285**,** 31590-602.

Cai, H., Reinisch, K. & Ferro-Novick, S. 2007. Coats, tethers, Rabs, and SNAREs work together to mediate the intracellular destination of a transport vesicle. *Dev Cell,* 12**,** 671-82.

Carney, D. S., Davies, B. A. & Horazdovsky, B. F. 2006. Vps9 domain-containing proteins: activators of Rab5 GTPases from yeast to neurons. *Trends Cell Biol,* 16**,** 27-35.

Carpanini, S. M., Mckie, L., Thomson, D., Wright, A. K., Gordon, S. L., Roche, S. L., Handley, M. T., Morrison, H., Brownstein, D., Wishart, T. M., Cousin, M. A., Gillingwater, T. H., Aligianis, I. A. & Jackson, I. J. 2014. A novel mouse model of Warburg Micro syndrome reveals roles for RAB18 in eye development and organisation of the neuronal cytoskeleton. *Dis Model Mech,* 7**,** 711-22.

Christoforidis, S., Mcbride, H. M., Burgoyne, R. D. & Zerial, M. 1999. The Rab5 effector EEA1 is a core component of endosome docking. *Nature,* 397**,** 621-5.

Cox, J., Hein, M. Y., Luber, C. A., Paron, I., Nagaraj, N. & Mann, M. 2014. Accurate proteome-wide label-free quantification by delayed normalization and maximal peptide ratio extraction, termed MaxLFQ. *Mol Cell Proteomics,* 13**,** 2513-26.

Dejgaard, S. Y., Murshid, A., Erman, A., Kizilay, O., Verbich, D., Lodge, R., Dejgaard, K., Ly-Hartig, T. B., Pepperkok, R., Simpson, J. C. & Presley, J. F. 2008. Rab18 and Rab43 have key roles in ER-Golgi trafficking. *J Cell Sci,* 121**,** 2768-81.

Dilcher, M., Veith, B., Chidambaram, S., Hartmann, E., Schmitt, H. D. & Fischer Von Mollard, G. 2003. Use1p is a yeast SNARE protein required for retrograde traffic to the ER. *EMBO J,* 22**,** 3664-74.

Eastman, S. W., Yassaee, M. & Bieniasz, P. D. 2009. A role for ubiquitin ligases and Spartin/SPG20 in lipid droplet turnover. *J Cell Biol,* 184**,** 881-94.

Edwards, T. L., Clowes, V. E., Tsang, H. T., Connell, J. W., Sanderson, C. M., Luzio, J. P. & Reid, E. 2009. Endogenous spartin (SPG20) is recruited to endosomes and lipid droplets and interacts with the ubiquitin E3 ligases AIP4 and AIP5. *Biochem J,* 423**,** 31-9.

Feldmann, A., Bekbulat, F., Huesmann, H., Ulbrich, S., Tatzelt, J., Behl, C. & Kern, A. 2017. The RAB GTPase RAB18 modulates macroautophagy and proteostasis. *Biochem Biophys Res Commun,* 486**,** 738-743.

Fukuda, M., Kanno, E., Ishibashi, K. & Itoh, T. 2008. Large scale screening for novel rab effectors reveals unexpected broad Rab binding specificity. *Mol Cell Proteomics,* 7**,** 1031-42.

Galea, G., Bexiga, M. G., Panarella, A., O'neill, E. D. & Simpson, J. C. 2015. A high-content screening microscopy approach to dissect the role of Rab proteins in Golgi-to-ER retrograde trafficking. *J Cell Sci,* 128**,** 2339-49.

Ge, L., Melville, D., Zhang, M. & Schekman, R. 2013. The ER-Golgi intermediate compartment is a key membrane source for the LC3 lipidation step of autophagosome biogenesis. *Elife,* 2**,** e00947.

Gerondopoulos, A., Bastos, R. N., Yoshimura, S., Anderson, R., Carpanini, S., Aligianis, I., Handley, M. T. & Barr, F. A. 2014. Rab18 and a Rab18 GEF complex are required for normal ER structure. *J Cell Biol,* 205**,** 707-20.

Gillingham, A. K., Bertram, J., Begum, F. & Munro, S. 2019. In vivo identification of GTPase interactors by mitochondrial relocalization and proximity biotinylation. *Elife,* 8.

Gillingham, A. K., Sinka, R., Torres, I. L., Lilley, K. S. & Munro, S. 2014. Toward a comprehensive map of the effectors of rab GTPases. *Dev Cell,* 31**,** 358-73.

Handley, M. & Sheridan, E. 2018. RAB18 Deficiency. *In:* ADAM, M. P., ARDINGER, H. H., PAGON, R. A., WALLACE, S. E., BEAN, L. J. H., STEPHENS, K. & AMEMIYA, A. (eds.) *GeneReviews((R)).* Seattle (WA).

Handley, M. T., Carpanini, S. M., Mali, G. R., Sidjanin, D. J., Aligianis, I. A., Jackson, I. J. & Fitzpatrick, D. R. 2015. Warburg Micro syndrome is caused by RAB18 deficiency or dysregulation. *Open Biol,* 5**,** 150047.

Hendershott, M. C. & Vale, R. D. 2014. Regulation of microtubule minus-end dynamics by CAMSAPs and Patronin. *Proc Natl Acad Sci U S A,* 111**,** 5860-5.

Hirose, H., Arasaki, K., Dohmae, N., Takio, K., Hatsuzawa, K., Nagahama, M., Tani, K., Yamamoto, A., Tohyama, M. & Tagaya, M. 2004. Implication of ZW10 in membrane trafficking between the endoplasmic reticulum and Golgi. *EMBO J,* 23**,** 1267-78.

Hueschen, C. L., Kenny, S. J., Xu, K. & Dumont, S. 2017. NuMA recruits dynein activity to microtubule minus-ends at mitosis. *Elife,* 6.

Jia, D., Zhang, J. S., Li, F., Wang, J., Deng, Z., White, M. A., Osborne, D. G., Phillips-Krawczak, C., Gomez, T. S., Li, H., Singla, A., Burstein, E., Billadeau, D. D. & Rosen, M. K. 2016. Structural and mechanistic insights into regulation of the retromer coat by TBC1d5. *Nat Commun,* 7**,** 13305.

Jimenez-Orgaz, A., Kvainickas, A., Nagele, H., Denner, J., Eimer, S., Dengjel, J. & Steinberg, F. 2018. Control of RAB7 activity and localization through the retromer-TBC1D5 complex enables RAB7-dependent mitophagy. *EMBO J,* 37**,** 235-254.

Jin, J., Sison, K., Li, C., Tian, R., Wnuk, M., Sung, H. K., Jeansson, M., Zhang, C., Tucholska, M., Jones, N., Kerjaschki, D., Shibuya, M., Fantus, I. G., Nagy, A., Gerber, H. P., Ferrara, N., Pawson, T. & Quaggin, S. E. 2012. Soluble FLT1 binds lipid microdomains in podocytes to control cell morphology and glomerular barrier function. *Cell,* 151**,** 384-99.

Johansson, M., Lehto, M., Tanhuanpaa, K., Cover, T. L. & Olkkonen, V. M. 2005. The oxysterol-binding protein homologue ORP1L interacts with Rab7 and alters functional properties of late endocytic compartments. *Mol Biol Cell,* 16**,** 5480-92.
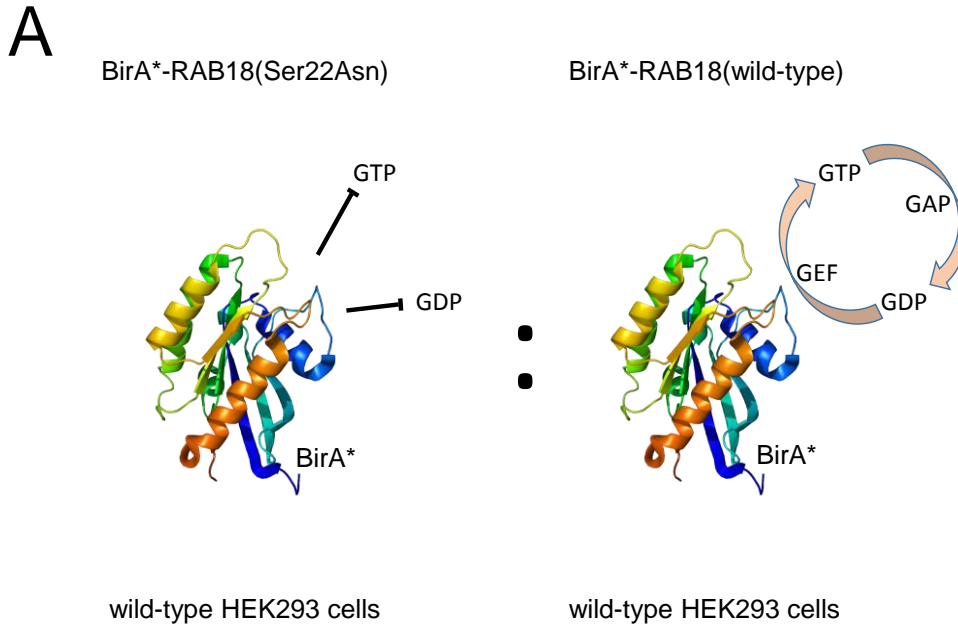
1134 Joshi, D. C. & Bakowska, J. C. 2011. SPG20 protein spartin associates with
1135 cardiolipin via its plant-related senescence domain and regulates
1136 mitochondrial Ca2+ homeostasis. *PLoS One,* 6**,** e19290.

1137 Kamena, F., Diefenbacher, M., Kilchert, C., Schwarz, H. & Spang, A. 2008. Ypt1p is
1138 essential for retrograde Golgi-ER transport and for Golgi maintenance in S.
1139 cerevisiae. *J Cell Sci,* 121**,** 1293-302.

1140 Kelley, L. A., Mezulis, S., Yates, C. M., Wass, M. N. & Sternberg, M. J. 2015. The
1141 Phyre2 web portal for protein modeling, prediction and analysis. *Nat Protoc,*
1142 10**,** 845-58.

1143 Kim, D. I., Jensen, S. C., Noble, K. A., Kc, B., Roux, K. H., Motamedchaboki, K. &
1144 Roux, K. J. 2016. An improved smaller biotin ligase for BioID proximity
1145 labeling. *Mol Biol Cell,* 27**,** 1188-96.

1146 Kumar, D., Golchoubian, B., Belevich, I., Jokitalo, E. & Schlaitz, A. L. 2019. REEP3
1147 and REEP4 determine the tubular morphology of the endoplasmic reticulum
1148 during mitosis. *Mol Biol Cell,* 30**,** 1377-1389.

1149 Lamber, E. P., Siedenburg, A. C. & Barr, F. A. 2019. Rab regulation by GEFs and
1150 GAPs during membrane traffic. *Curr Opin Cell Biol,* 59**,** 34-39.

1151 Langemeyer, L., Perz, A., Kummel, D. & Ungermann, C. 2018. A guanine nucleotide
1152 exchange factor (GEF) limits Rab GTPase-driven membrane fusion. *J Biol*
1153 *Chem,* 293**,** 731-739.

1154 Lees, J. A., Messa, M., Sun, E. W., Wheeler, H., Torta, F., Wenk, M. R., De Camilli,
1155 P. & Reinisch, K. M. 2017. Lipid transport by TMEM24 at ER-plasma
1156 membrane contacts regulates pulsatile insulin secretion. *Science,* 355.

1157 Lewis, M. J. & Pelham, H. R. 1996. SNARE-mediated retrograde traffic from the
1158 Golgi complex to the endoplasmic reticulum. *Cell,* 85**,** 205-15.

1159 Lewis, M. J., Rayner, J. C. & Pelham, H. R. 1997. A novel SNARE complex
1160 implicated in vesicle fusion with the endoplasmic reticulum. *EMBO J,* 16**,**
1161 3017-24.

1162 Li, C., Luo, X., Zhao, S., Siu, G. K., Liang, Y., Chan, H. C., Satoh, A. & Yu, S. S.
1163 2017. COPI-TRAPPII activates Rab18 and regulates its lipid droplet
1164 association. *EMBO J,* 36**,** 441-457.

1165 Li, D., Zhao, Y. G., Li, D., Zhao, H., Huang, J., Miao, G., Feng, D., Liu, P., Li, D. &
1166 Zhang, H. 2019. The ER-Localized Protein DFCP1 Modulates ER-Lipid
1167 Droplet Contact Formation. *Cell Rep,* 27**,** 343-358 e5.

1168 Liegel, R. P., Handley, M. T., Ronchetti, A., Brown, S., Langemeyer, L., Linford, A.,
1169 Chang, B., Morris-Rosendahl, D. J., Carpanini, S., Posmyk, R., Harthill, V.,
1170 Sheridan, E., Abdel-Salam, G. M., Terhal, P. A., Faravelli, F., Accorsi, P.,
1171 Giordano, L., Pinelli, L., Hartmann, B., Ebert, A. D., Barr, F. A., Aligianis, I. A.
1172 & Sidjanin, D. J. 2013. Loss-of-function mutations in TBC1D20 cause
1173 cataracts and male infertility in blind sterile mice and Warburg micro
1174 syndrome in humans. *Am J Hum Genet,* 93**,** 1001-14.

1175 Lind, G. E., Raiborg, C., Danielsen, S. A., Rognum, T. O., Thiis-Evensen, E., Hoff,
1176 G., Nesbakken, A., Stenmark, H. & Lothe, R. A. 2011. SPG20, a novel

1177   biomarker for early detection of colorectal cancer, encodes a regulator of
1178   cytokinesis. *Oncogene,* 30**,** 3967-78.

1179   Liu, X., Salokas, K., Tamene, F., Jiu, Y., Weldatsadik, R. G., Ohman, T. & Varjosalo,
1180   M. 2018. An AP-MS- and BioID-compatible MAC-tag enables comprehensive
1181   mapping of protein interactions and subcellular localizations. *Nat Commun,* 9**,**
1182   1188.

1183   Martin, S., Driessen, K., Nixon, S. J., Zerial, M. & Parton, R. G. 2005. Regulated
1184   localization of Rab18 to lipid droplets: effects of lipolytic stimulation and
1185   inhibition of lipid droplet catabolism. *J Biol Chem,* 280**,** 42325-35.

1186   Nahm, M., Lee, M. J., Parkinson, W., Lee, M., Kim, H., Kim, Y. J., Kim, S., Cho, Y.
1187   S., Min, B. M., Bae, Y. C., Broadie, K. & Lee, S. 2013. Spartin regulates
1188   synaptic growth and neuronal survival by inhibiting BMP-mediated
1189   microtubule stabilization. *Neuron,* 77**,** 680-95.

1190   Nakajima, K., Hirose, H., Taniguchi, M., Kurashina, H., Arasaki, K., Nagahama, M.,
1191   Tani, K., Yamamoto, A. & Tagaya, M. 2004. Involvement of BNIP1 in
1192   apoptosis and endoplasmic reticulum membrane fusion. *EMBO J,* 23**,** 3216-
1193   26.

1194   Nakamura, H., Yamashita, N., Kimura, A., Kimura, Y., Hirano, H., Makihara, H.,
1195   Kawamoto, Y., Jitsuki-Takahashi, A., Yonezaki, K., Takase, K., Miyazaki, T.,
1196   Nakamura, F., Tanaka, F. & Goshima, Y. 2016. Comprehensive behavioral
1197   study and proteomic analyses of CRMP2-deficient mice. *Genes Cells,* 21**,**
1198   1059-1079.

1199   Nicholson, J. M., Macedo, J. C., Mattingly, A. J., Wangsa, D., Camps, J., Lima, V.,
1200   Gomes, A. M., Doria, S., Ried, T., Logarinho, E. & Cimini, D. 2015.
1201   Chromosome mis-segregation and cytokinesis failure in trisomic human cells.
1202   *Elife,* 4.

1203   Ong, W. Y., Ng, M. P., Loke, S. Y., Jin, S., Wu, Y. J., Tanaka, K. & Wong, P. T.
1204   2013. Comprehensive gene expression profiling reveals synergistic functional
1205   networks in cerebral vessels after hypertension or hypercholesterolemia.
1206   *PLoS One,* 8**,** e68335.

1207   Ozeki, S., Cheng, J., Tauchi-Sato, K., Hatano, N., Taniguchi, H. & Fujimoto, T. 2005.
1208   Rab18 localizes to lipid droplets and induces their close apposition to the
1209   endoplasmic reticulum-derived membrane. *J Cell Sci,* 118**,** 2601-11.

1210   Perez-Riverol, Y., Csordas, A., Bai, J., Bernal-Llinares, M., Hewapathirana, S.,
1211   Kundu, D. J., Inuganti, A., Griss, J., Mayer, G., Eisenacher, M., Perez, E.,
1212   Uszkoreit, J., Pfeuffer, J., Sachsenberg, T., Yilmaz, S., Tiwary, S., Cox, J.,
1213   Audain, E., Walzer, M., Jarnuczak, A. F., Ternent, T., Brazma, A. & Vizcaino,
1214   J. A. 2019. The PRIDE database and related tools and resources in 2019:
1215   improving support for quantification data. *Nucleic Acids Res,* 47**,** D442-D450.

1216   Petkovic, M., Jemaiel, A., Daste, F., Specht, C. G., Izeddin, I., Vorkel, D., Verbavatz,
1217   J. M., Darzacq, X., Triller, A., Pfenninger, K. H., Tareste, D., Jackson, C. L. &
1218   Galli, T. 2014. The SNARE Sec22b has a non-fusogenic function in plasma
1219   membrane expansion. *Nat Cell Biol,* 16**,** 434-44.

1220   Pulido, M. R., Diaz-Ruiz, A., Jimenez-Gomez, Y., Garcia-Navarro, S., Gracia-
1221   Navarro, F., Tinahones, F., Lopez-Miranda, J., Fruhbeck, G., Vazquez-

Martinez, R. & Malagon, M. M. 2011. Rab18 dynamics in adipocytes in relation to lipogenesis, lipolysis and obesity. *PLoS One,* 6**,** e22931.

Raiborg, C., Wenzel, E. M., Pedersen, N. M., Olsvik, H., Schink, K. O., Schultz, S. W., Vietri, M., Nisi, V., Bucci, C., Brech, A., Johansen, T. & Stenmark, H. 2015. Repeated ER-endosome contacts promote endosome translocation and neurite outgrowth. *Nature,* 520**,** 234-8.

Ran, F. A., Hsu, P. D., Wright, J., Agarwala, V., Scott, D. A. & Zhang, F. 2013. Genome engineering using the CRISPR-Cas9 system. *Nat Protoc,* 8**,** 2281-2308.

Renvoise, B., Stadler, J., Singh, R., Bakowska, J. C. & Blackstone, C. 2012. Spg20-/- mice reveal multimodal functions for Troyer syndrome protein spartin in lipid droplet maintenance, cytokinesis and BMP signaling. *Hum Mol Genet,* 21**,** 3604-18.

Richter, K. N., Revelo, N. H., Seitz, K. J., Helm, M. S., Sarkar, D., Saleeb, R. S., D'este, E., Eberle, J., Wagner, E., Vogl, C., Lazaro, D. F., Richter, F., Coy-Vergara, J., Coceano, G., Boyden, E. S., Duncan, R. R., Hell, S. W., Lauterbach, M. A., Lehnart, S. E., Moser, T., Outeiro, T. F., Rehling, P., Schwappach, B., Testa, I., Zapiec, B. & Rizzoli, S. O. 2018. Glyoxal as an alternative fixative to formaldehyde in immunostaining and super-resolution microscopy. *EMBO J,* 37**,** 139-159.

Ring, J., Rockenfeller, P., Abraham, C., Tadic, J., Poglitsch, M., Schimmel, K., Westermayer, J., Schauer, S., Achleitner, B., Schimpel, C., Moitzi, B., Rechberger, G. N., Sigrist, S. J., Carmona-Gutierrez, D., Kroemer, G., Buttner, S., Eisenberg, T. & Madeo, F. 2017. Mitochondrial energy metabolism is required for lifespan extension by the spastic paraplegia-associated protein spartin. *Microb Cell,* 4**,** 411-422.

Rocha, N., Kuijl, C., Van Der Kant, R., Janssen, L., Houben, D., Janssen, H., Zwart, W. & Neefjes, J. 2009. Cholesterol sensor ORP1L contacts the ER protein VAP to control Rab7-RILP-p150 Glued and late endosome positioning. *J Cell Biol,* 185**,** 1209-25.

Roux, K. J., Kim, D. I., Burke, B. & May, D. G. 2018. BioID: A Screen for Protein-Protein Interactions. *Curr Protoc Protein Sci,* 91**,** 19 23 1-19 23 15.

Roux, K. J., Kim, D. I., Raida, M. & Burke, B. 2012. A promiscuous biotin ligase fusion protein identifies proximal and interacting proteins in mammalian cells. *J Cell Biol,* 196**,** 801-10.

Schlaitz, A. L., Thompson, J., Wong, C. C., Yates, J. R., 3rd & Heald, R. 2013. REEP3/4 ensure endoplasmic reticulum clearance from metaphase chromatin and proper nuclear envelope architecture. *Dev Cell,* 26**,** 315-23.

Seaman, M. N., Harbour, M. E., Tattersall, D., Read, E. & Bright, N. 2009. Membrane recruitment of the cargo-selective retromer subcomplex is catalysed by the small GTPase Rab7 and inhibited by the Rab-GAP TBC1D5. *J Cell Sci,* 122**,** 2371-82.

Sidjanin, D. J., Park, A. K., Ronchetti, A., Martins, J. & Jackson, W. T. 2016. TBC1D20 mediates autophagy as a key regulator of autophagosome maturation. *Autophagy***,** 1-17.

1267 Silve, S., Dupuy, P. H., Labit-Lebouteiller, C., Kaghad, M., Chalon, P., Rahier, A.,
1268 Taton, M., Lupker, J., Shire, D. & Loison, G. 1996. Emopamil-binding protein,
1269 a mammalian protein that binds a series of structurally diverse
1270 neuroprotective agents, exhibits delta8-delta7 sterol isomerase activity in
1271 yeast. *J Biol Chem,* 271**,** 22434-40.

1272 Sobajima, T., Yoshimura, S. I., Maeda, T., Miyata, H., Miyoshi, E. & Harada, A.
1273 2018. The Rab11-binding protein RELCH/KIAA1468 controls intracellular
1274 cholesterol distribution. *J Cell Biol,* 217**,** 1777-1796.

1275 Spang, A. 2012. The DSL1 complex: the smallest but not the least CATCHR. *Traffic,*
1276 13**,** 908-13.

1277 Spang, N., Feldmann, A., Huesmann, H., Bekbulat, F., Schmitt, V., Hiebel, C.,
1278 Koziollek-Drechsler, I., Clement, A. M., Moosmann, B., Jung, J., Behrends,
1279 C., Dikic, I., Kern, A. & Behl, C. 2014. RAB3GAP1 and RAB3GAP2 modulate
1280 basal and rapamycin-induced autophagy. *Autophagy,* 10**,** 2297-309.

1281 Tagaya, M., Arasaki, K., Inoue, H. & Kimura, H. 2014. Moonlighting functions of the
1282 NRZ (mammalian Dsl1) complex. *Front Cell Dev Biol,* 2**,** 25.

1283 Tinti, M., Johnson, C., Toth, R., Ferrier, D. E. & Mackintosh, C. 2012. Evolution of
1284 signal multiplexing by 14-3-3-binding 2R-ohnologue protein families in the
1285 vertebrates. *Open Biol,* 2**,** 120103.

1286 Tsang, H. T., Edwards, T. L., Wang, X., Connell, J. W., Davies, R. J., Durrington, H.
1287 J., O'kane, C. J., Luzio, J. P. & Reid, E. 2009. The hereditary spastic
1288 paraplegia proteins NIPA1, spastin and spartin are inhibitors of mammalian
1289 BMP signalling. *Hum Mol Genet,* 18**,** 3805-21.

1290 Urnavicius, L., Zhang, K., Diamant, A. G., Motz, C., Schlager, M. A., Yu, M., Patel, N.
1291 A., Robinson, C. V. & Carter, A. P. 2015. The structure of the dynactin
1292 complex and its interaction with dynein. *Science,* 347**,** 1441-1446.

1293 Vazquez-Martinez, R., Cruz-Garcia, D., Duran-Prado, M., Peinado, J. R., Castano, J.
1294 P. & Malagon, M. M. 2007. Rab18 inhibits secretory activity in neuroendocrine
1295 cells by interacting with secretory granules. *Traffic,* 8**,** 867-82.

1296 Wang, H., Ma, Q., Qi, Y., Dong, J., Du, X., Rae, J., Wang, J., Wu, W. F., Brown, A.
1297 J., Parton, R. G., Wu, J. W. & Yang, H. 2019. ORP2 Delivers Cholesterol to
1298 the Plasma Membrane in Exchange for Phosphatidylinositol 4, 5-
1299 Bisphosphate (PI(4,5)P2). *Mol Cell,* 73**,** 458-473 e7.

1300 Wang, T., Li, L. & Hong, W. 2017. SNARE proteins in membrane trafficking. *Traffic,*
1301 18**,** 767-775.

1302 Whitfield, S. T., Burston, H. E., Bean, B. D., Raghuram, N., Maldonado-Baez, L.,
1303 Davey, M., Wendland, B. & Conibear, E. 2016. The alternate AP-1 adaptor
1304 subunit Apm2 interacts with the Mil1 regulatory protein and confers differential
1305 cargo sorting. *Mol Biol Cell,* 27**,** 588-98.

1306 Wickner, W. 2010. Membrane fusion: five lipids, four SNAREs, three chaperones,
1307 two nucleotides, and a Rab, all dancing in a ring on yeast vacuoles. *Annu Rev*
1308 *Cell Dev Biol,* 26**,** 115-36.

1309 Williams, C., Choudhury, R., Mckenzie, E. & Lowe, M. 2007. Targeting of the type II
1310   inositol polyphosphate 5-phosphatase INPP5B to the early secretory pathway.
1311   *J Cell Sci,* 120**,** 3941-51.

1312 Wu, H., Carvalho, P. & Voeltz, G. K. 2018. Here, there, and everywhere: The
1313   importance of ER membrane contact sites. *Science,* 361.

1314 Xu, D., Li, Y., Wu, L., Li, Y., Zhao, D., Yu, J., Huang, T., Ferguson, C., Parton, R. G.,
1315   Yang, H. & Li, P. 2018. Rab18 promotes lipid droplet (LD) growth by tethering
1316   the ER to LDs through SNARE and NRZ interactions. *J Cell Biol,* 217**,** 975-
1317   995.

1318 Yamaguchi, T., Dulubova, I., Min, S. W., Chen, X., Rizo, J. & Sudhof, T. C. 2002.
1319   Sly1 binds to Golgi and ER syntaxins via a conserved N-terminal peptide
1320   motif. *Dev Cell,* 2**,** 295-305.

1321 Yamamoto, Y., Yurugi, C. & Sakisaka, T. 2017. The number of the C-terminal
1322   transmembrane domains has the potency to specify subcellular localization of
1323   Sec22c. *Biochem Biophys Res Commun,* 487**,** 388-395.

1324 Zhang, T., Wong, S. H., Tang, B. L., Xu, Y. & Hong, W. 1999. Morphological and
1325   functional association of Sec22b/ERS-24 with the pre-Golgi intermediate
1326   compartment. *Mol Biol Cell,* 10**,** 435-53.

1327 Zhao, L. & Imperiale, M. J. 2017. Identification of Rab18 as an Essential Host Factor
1328   for BK Polyomavirus Infection Using a Whole-Genome RNA Interference
1329   Screen. *mSphere,* 2.

1330 Zhen, Y. & Stenmark, H. 2015. Cellular functions of Rab GTPases at a glance. *J Cell
1331   Sci,* 128**,** 3171-6.

1332

1333

A

BirA*-RAB18(Ser22Asn)

BirA*-RAB18(wild-type)

wild-type HEK293 cells

wild-type HEK293 cells

B

Protein	Ratio	Orthologue PPI (Gillingham et al., 2014)	Additional evidence	
SCFD2	0.00	Slh	Gillingham et al., 2019	RAB3GAP-dependent association in HeLa cells
ZW10	0.00	mit(1)15	Xu et al., 2018; Gillingham et al., 2019	
NBAS	0.00	rod	Xu et al., 2018; Gillingham et al., 2019	
CAMSAP1	0.04			
FAM134B	0.36			
RINT1	0.41	CG8605	Xu et al., 2018	
RAB3GAP2	1.58	rab3-GAP	Gerondopoulos et al., 2014	
RAB3GAP1	1.59	CG31935	Gerondopoulos et al., 2014	
TBC1D5	0.00	CG8449	Gillingham et al., 2019	TRAPPII-dependent association in HeLa cells
c15orf38	0.00			
SEC23IP	0.00			
ATP6AP2	0.29			
GORASP2	0.36			
GIGYF2	0.41			
TPR	0.41			
USP15	0.00			Present in HeLa dataset (n≥2)
TMPO	0.00			
ARFGAP3	0.20			
ARFGAP2	0.31			
SLK	0.34			
NUP153	0.39			
ATG2B	0.43			
SCFD1	0.45	Slh	Gillingham et al., 2019	
USE1	0.45		Xu et al., 2018	
TMX1	0.45			
CORO1B	0.47			
PREB	0.47			
SLC25A4	0.00			Absent in HeLa dataset (n≥2)
LUZP1	0.00			
DPYSL2	0.34		Nakamura et al., 2016	

1334

1335 **Figure 1. Nucleotide-binding-dependent RAB18-associations in HEK293 cells.**

1336 (A) Schematic to show BirA*-RAB18(Ser22Asn):BirA*-RAB18(WT) comparison.

1337 RAB18 crystal structure from RCSB PDB code 1X3S. (B) Table to show putative

1338 nucleotide-binding-dependent RAB18-associations with BirA*-

1339 RAB18(Ser22Asn):BirA*-RAB18(WT) association ratios <0.5. Proteins orthologous

1340 to interactors identified by Gillingham et al. (2014) are indicated. Previous studies

1341 providing supporting evidence for interactions are indicated. Proteins are grouped

1342 according to their attributes in the HeLa cell dataset (Figure 2 and Table S2).

1343 Association ratios were derived individually following normalization by total spectral

1344 counts per condition. The full dataset is provided in table S1.

1345

A

BirA*-RAB18(wild-type)　　　　BirA*-RAB18(wild-type)

GEF-null HeLa cells　　　　wild-type HeLa cells

B

$R^2=0.99$

C

All (457)
TRAPPII-dependent (133)
RAB3GAP-dependent (25)
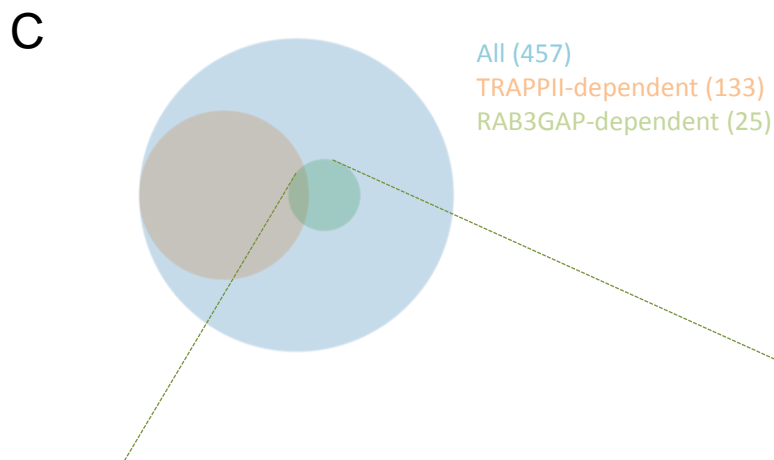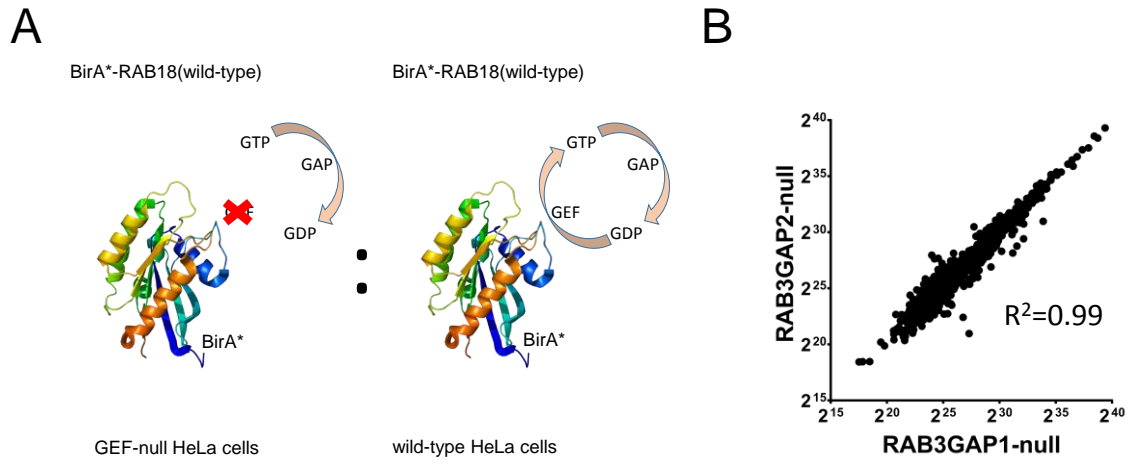
D

Protein	n	Ratio	Orthologue PPI (Gillingham et al., 2014)	Additional evidence	
CAMSAP1	3	0.26			Microtubule-associated/Membrane remodelling
REEP4	3	0.35		Tinti et al., 2012*	
BICD2	2	0.25	BicD	Gillingham et al., 2019	
SPG20	**2**	**0.42**	**CG12001**	**This study (Figure 4)**	
FAM134B	2	0.46			
ZW10	3	0.02	mit(1)15	Xu et al., 2018; Gillingham et al., 2019	Membrane tethering/docking
RINT1	3	0.16	CG8605	Xu et al., 2018	
NBAS	3	0.17	rod	Xu et al., 2018; Gillingham et al., 2019	
SCFD2	3	0.41	Slh	Gillingham et al., 2019	
SEC22A	**3**	**0.46**		**This study (Figure 5)**	
WFS1	2	0.00			
BNIP1	2	0.36		Xu et al., 2018	
STX18	2	0.40	Syx18	Xu et al., 2018	
TMCO4	**3**	**0.06**		**This study (Figure 6)**	Lipid modifying/mobilising
OSBPL2	3	0.35			
EBP	3	0.38			
INPP5B	2	0.00			
C2CD2L	2	0.22			
C2CD2	2	0.36			
RAB3GAP2	3	0.00	rab3-GAP	Gerondopoulos et al., 2014	Other
RAB3GAP1	3	0.01	CG31935	Gerondopoulos et al., 2014	
SSR3	3	0.49			
MFHAS1	2	0.00	lrrk		
TRIM13	2	0.29			
SCARA3	2	0.42			

1346

1347 **Figure 2. RAB3GAP-dependent RAB18-associations in HeLa cells.** (A)

1348 Schematic to show comparison of BirA*-RAB18(WT) in wild-type and guanine

1349 nucleotide exchange factor (GEF)-null cells. RAB18 crystal structure from RCSB

1350 PDB code 1X3S. (B) Plot to show correlation between non-zero LFQ intensities of

1351 individual proteins identified in samples purified from RAB3GAP1- and RAB3GAP2-

1352 null cells. (C) Venn diagram illustrating all RAB18-associations, TRAPPII-dependent

1353 interactions (TRAPPC9-null:wild-type association ratios <0.5) and RAB3GAP-

1354 dependent associations (RAB3GAP1/2-null:wild-type association ratios <0.5). (D)

1355 Table to show putative RAB18-associations with RAB3GAP1/2-null:wild-type

1356 association ratios <0.5. Proteins orthologous to interactors identified by Gillingham et

1357 al. (2014) are indicated. Previous studies providing supporting evidence for

1358 interactions are indicated. Proteins are grouped according to their reported functions.

1359 Association ratios were derived individually following normalization by RAB18 LFQ

1360 intensity in each replicate experiment. The full dataset is provided in table S2.

1361
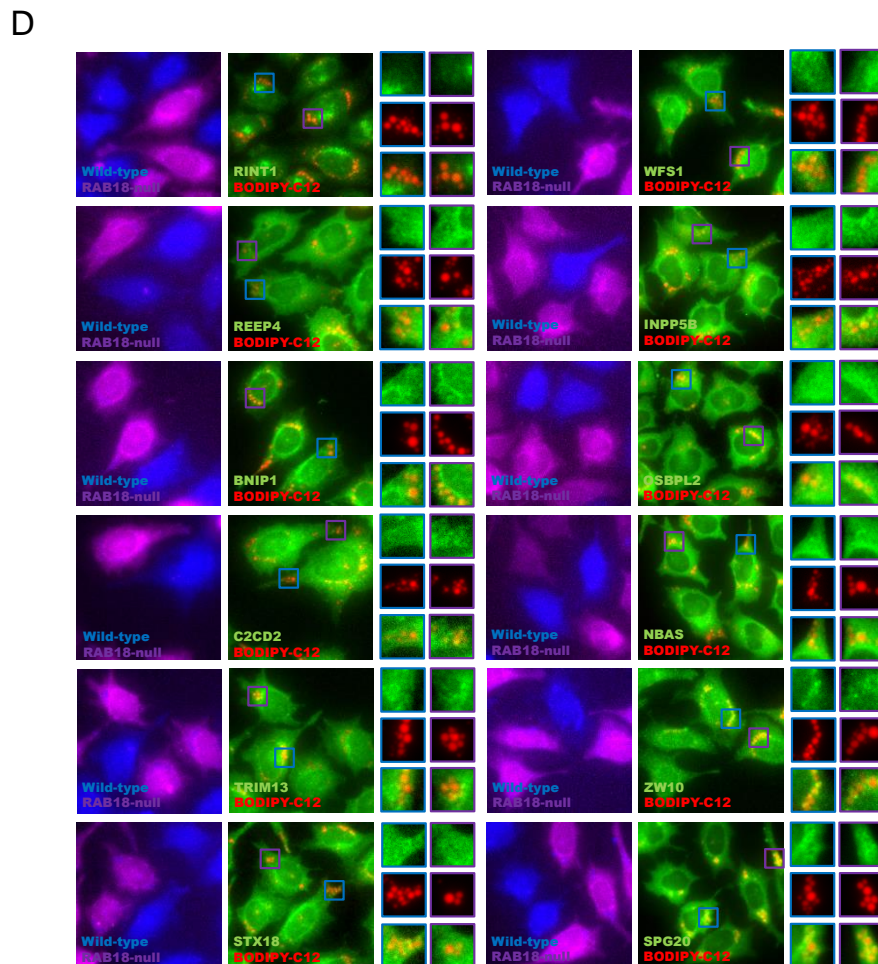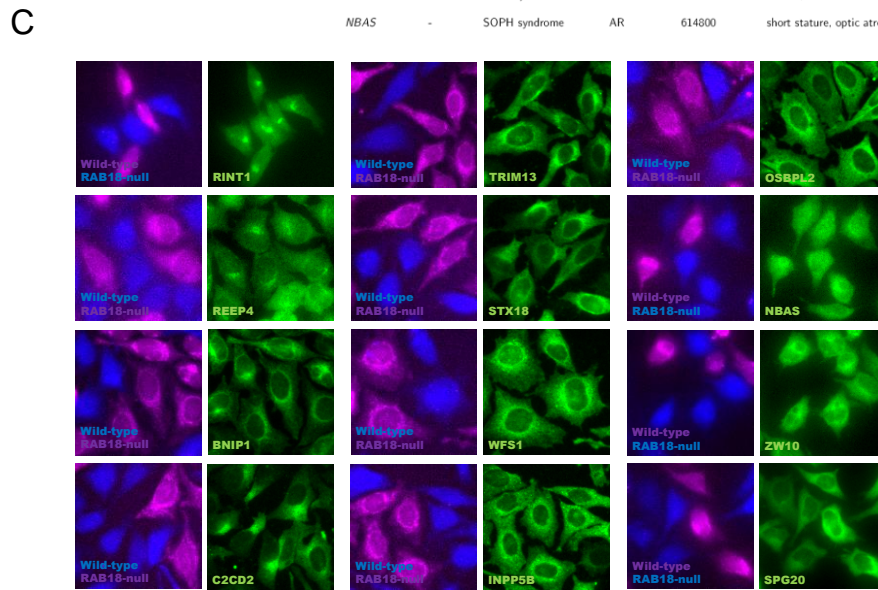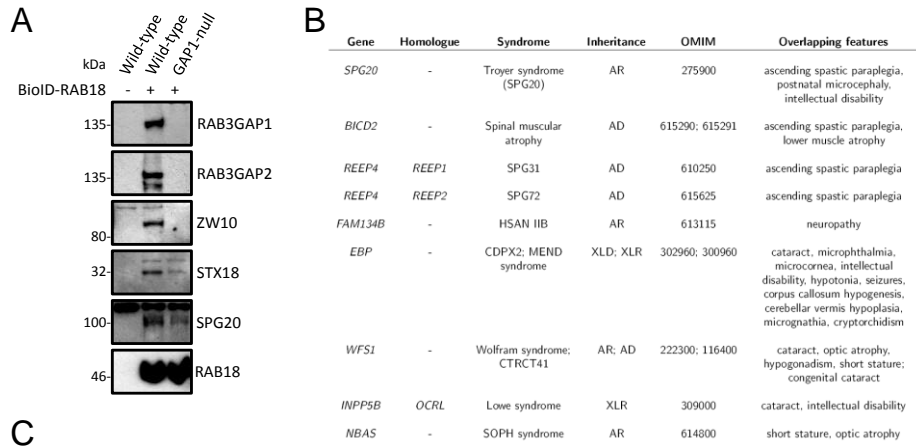
1363 **Figure 3. Initial validation of RAB3GAP-dependent RAB18-associations in**

1364 **HeLa cells.** (A) Western blotting of samples purified from wild-type and RAB3GAP1-

1365 null cells in an independent BioID experiment. Levels of selected proteins are

1366 consistent with association ratios in Figure 1C. (B) Table to show diseases with

1367 features overlapping those of Warburg Micro syndrome linked to genes encoding

1368 putative effector proteins or their homologues. (C) Comparative fluorescence

1369 microscopy of selected RAB18-associated proteins in wild-type and RAB18-null

1370 HeLa cells. Cells of different genotypes were labelled with CellTrace-Violet and

1371 CellTrace-Far Red reagents, corresponding to blue and magenta channels

1372 respectively. Cells were stained with antibodies against indicated proteins in green

1373 channel panels. (D) Comparative fluorescence microscopy of selected RAB18-

1374 associated proteins in lipid-loaded wild-type and RAB18-null HeLa cells. Cells were

1375 stained as above but were treated for 15 hours with 200µM oleic acid, 1µg/ml

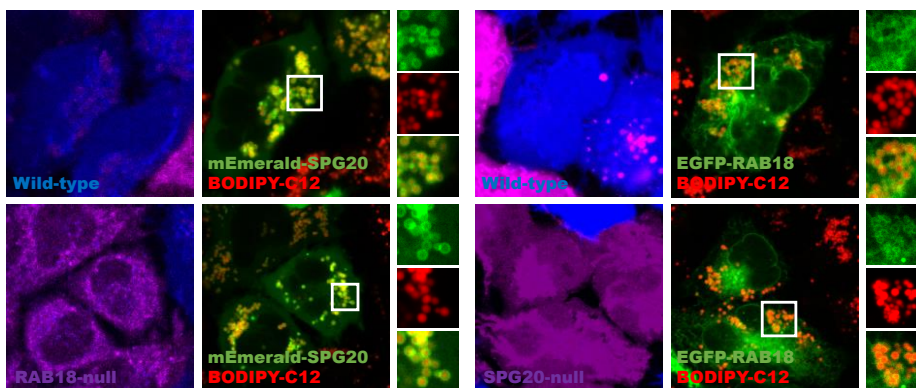1376 BODIPY-558/568-C12 (Red channel) prior to fixation.

1377

1378
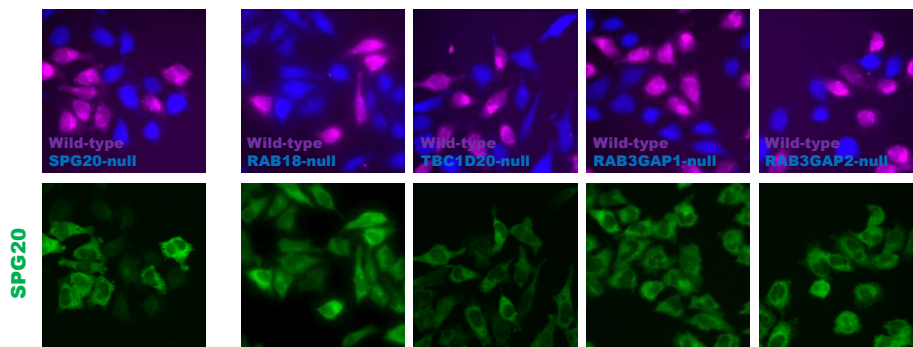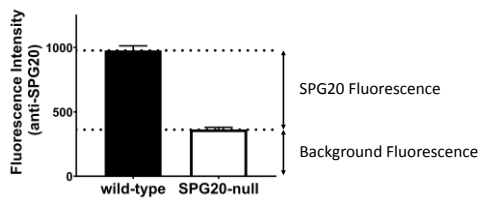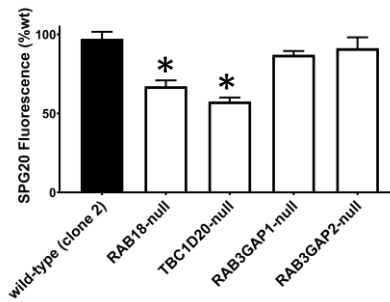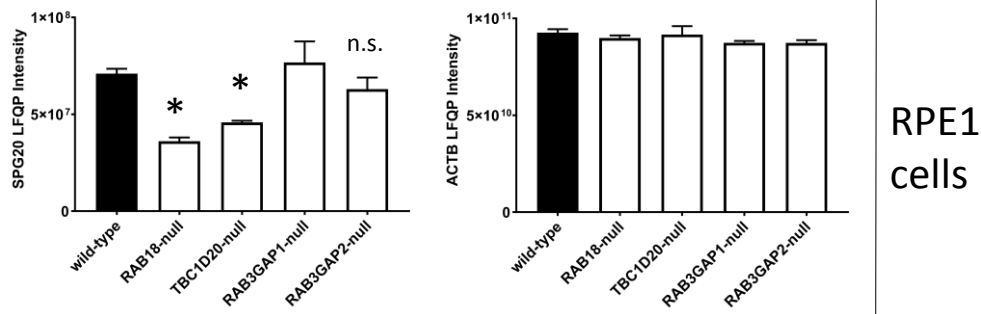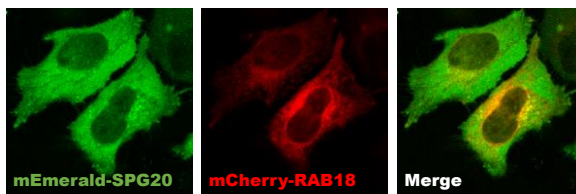
1379 **Figure 4. Levels of SPG20 are significantly reduced in RAB18-null and**

1380 **TBC1D20-null HeLa and RPE1 cells.** (A) Comparative fluorescence microscopy of

1381 SPG20 in wild-type and mutant HeLa cell lines. Wild-type and mutant cells of the

1382 indicated genotypes were labelled with CellTrace-Far Red and CellTrace-Violet and

1383 reagents respectively (magenta and blue channels). Cells were stained with an

1384 antibody against SPG20 (green channel) (B) Quantification of SPG20 fluorescence

1385 in wild-type cells by direct comparison with SPG20-null cells. (C) Quantification of

1386 SPG20 fluorescence (%wt) in cells of different genotypes. Data were derived from

1387 analysis of at least 18 frames – each containing >5 wild-type and >5 mutant cells –

1388 per genotype. *p<0.001. (D) LFQ intensities for SPG20 (Q8N0X7) and β-Actin

1389 (P60709) in whole-cell lysates of RPE1 cells of the indicated genotypes. n=3;

1390 *p<0.05 following FDR correction. Full dataset provided in table S3. Error bars

1391 represent s.e.m. (E) Confocal micrograph to show localization of exogenous

1392 mEmerald-SPG20 (Green) and mCherry-RAB18 (Red) in HeLa cells. (F) Confocal

1393 micrographs to show localization of exogenous mEmerald-SPG20 (Green; left

1394 panels) and EGFP-RAB18 (Green; right panels) in HeLa cells loaded with 200μM

1395 oleic acid, 1μg/ml BODIPY-558/568-C12 (Red channel). Wild-type and mutant cells

1396 of the indicated genotypes were labelled with CellTrace-Violet and CellTrace-Far

1397 Red reagents respectively (magenta and blue channels).

1398
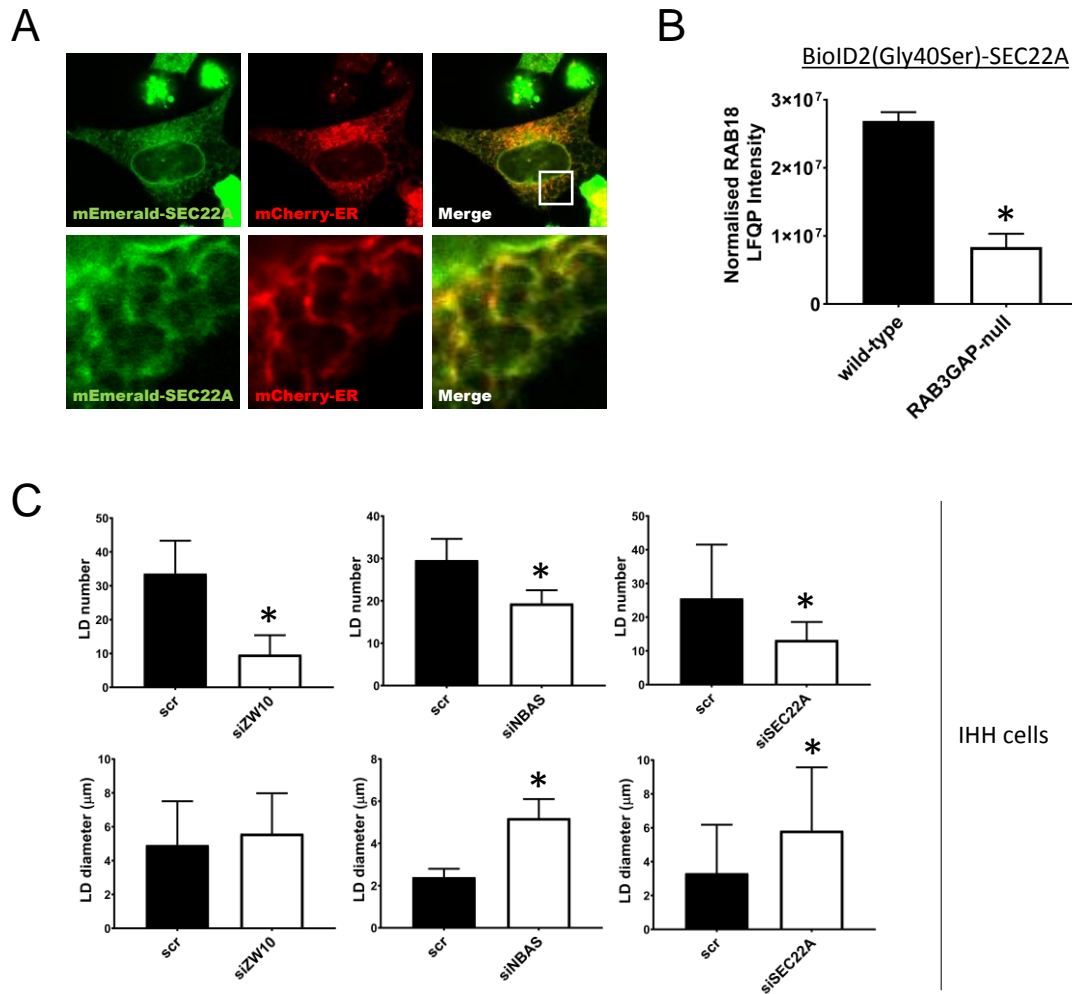
1399

Figure 5. SEC22A associates with RAB18 and influences LD morphology. (A) Confocal micrograph to show overlapping localization of exogenous mEmerald-SEC22A (Green) and mCherry-ER (Red) in HeLa cells. (B) RAB18 LFQ intensities from a reciprocal BioID experiment showing a reduced association between BioID2(Gly40Ser)-SEC22A and endogenous RAB18 in RAB3GAP-null compared to wild-type HeLa cells. Data were adjusted to account for non-specific binding of RAB18 to beads and normalized by SEC22A LFQ intensities in each replicate experiment. Error bars represent s.e.m. Data for other BioID2(Gly40Ser)-SEC22A-associated proteins are provided in table S5. (C) Bar graphs to show effects of ZW10, NBAS and SEC22A knockdowns on lipid droplet number and diameter. siRNA-treated IHH cells were loaded with 200nM BSA-conjugated oleate, fixed and stained with BODIPY and DAPI, and imaged. Images were analysed using ImageJ. Data are derived from measurements from >100 cells/condition and are representative of three independent experiments. Error bars represent SD. *p<0.001
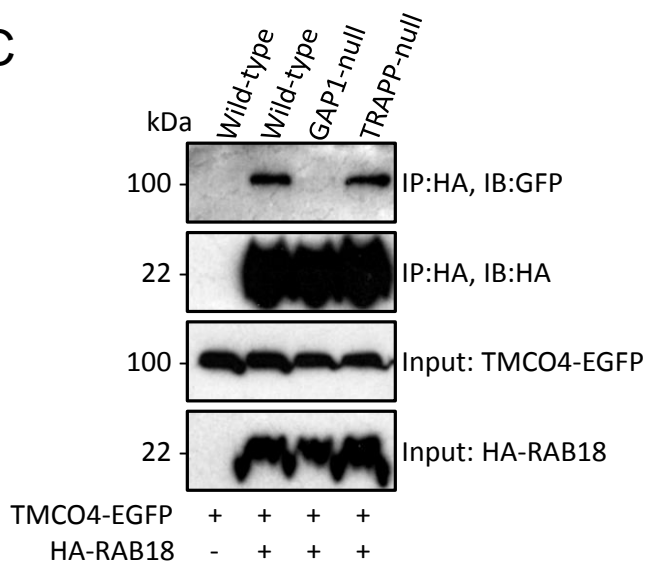
A

B

C

1414
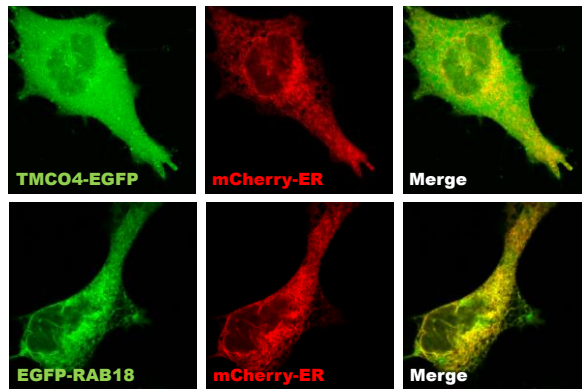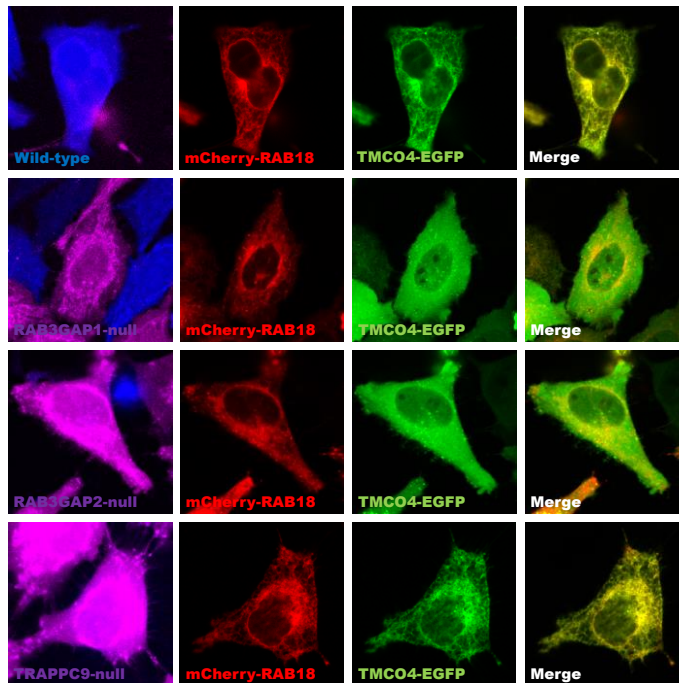
1415   **Figure 6. mCherry-RAB18 recruits TMCO4-EGFP to the ER membrane in a**

1416   **RAB3GAP-dependent manner.** (A) Confocal micrographs to show diffuse

1417   localization of exogenous TMCO4-EGFP (Green) compared to mCherry-ER (Red)

1418   and overlapping localization of exogenous EGFP-RAB18 (Green) and mCherry-ER

1419   in HeLa cells. (B) Confocal micrographs to show localization of exogenous mCherry-

1420   RAB18 and TMCO4-EGFP in wild-type cells and in mutant cells of different

1421   genotypes. Wild-type and mutant cells of the indicated genotypes were labelled with

1422   CellTrace-Violet and CellTrace-Far Red reagents respectively (magenta and blue

1423   channels). (C) Immunoprecipitation of exogenous HA-RAB18 from HeLa cells of

1424   different genotypes. Cells were transfected with the indicated constructs and lysed

1425   24 hours post-transfection. Anti-HA immunoprecipitates and input samples were

1426   subjected to SDS-PAGE and immunostaining for HA and GFP.

1427
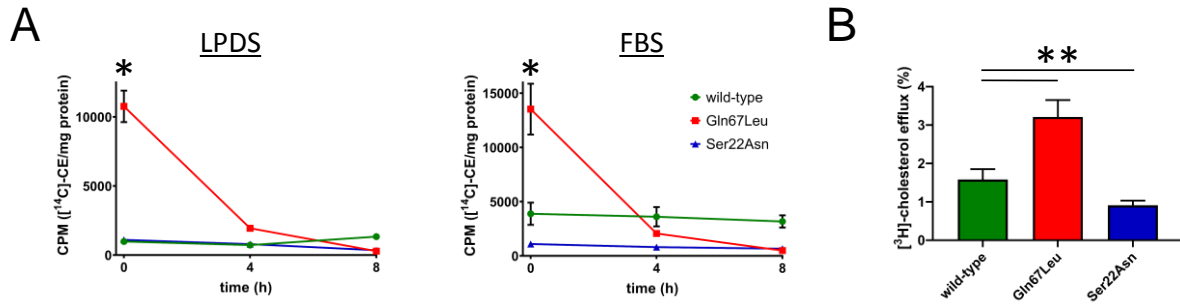
1428

Figure 7. RAB18 is involved in the mobilization of cholesterol. (A) Plots to show cholesteryl ester (CE) loading and efflux. CHO cells, stably expressing RAB18(WT), RAB18(Gln67Leu) and RAB18(Ser22Asn), were incubated with [^{14}C]-oleate, for 24 hours, in the presence of lipoprotein depleted serum (LPDS)(Left panel) or FBS (Right panel). Following lipid extraction, thin layer chromatography (TLC) was used to separate CE, and radioactivity was measured by scintillation counting. Measurements were made at t=0 and at 4 and 8 hours following the addition of 50µg/ml high density lipoprotein (HDL) to the cells. (B) Bar graph to show cholesterol efflux. The CHO cells were incubated with [^{3}H]-cholesterol, for 24 hours, in the presence of FBS. After washing, they were then incubated with 25µg/ml apolipoprotein A-I for 5 hours. The quantity of [^{3}H]-cholesterol in the media is shown as a percentage of the total cellular radioactivity (mean+/-SD). *p<0.01, **p<0.001.